A Preliminary Thermochemical Model of the Australian Lithosphere

By

Byron Gear

A thesis submitted to Macquarie University
for the degree of Master of Research
Department of Earth and Planetary Sciences

Australian Research Council Centre of Excellence for
Core to Crust Fluid Systems (CCFS) and GEMOC

November 2017

Examiner's Copy

Typeset in $\LaTeX\,2_\varepsilon$.

Acknowledgements

The first person I need to thank is my supervisor, Dr. Juan Carlos Afonso, for his endless support, motivation, patience and constructive feedback. Without him this research project would not exist. I would like to show a special appreciation for the post-graduate students at Macquarie University who helped me with countless issues I brought to them, Farshad Salajegheh, Mehdi Tork-Qashqai and Maria Constanza Manassero.

I am grateful to Kazunori Yoshizawa, Earth and Planetary Dynamics, Hokkaido University, Sapporo, Japan for providing the dispersion data used as the main dataset in this work. And also to Derrick Hasterok, Department of Earth Sciences, University of Adelaide, Australia for providing me with his surface heat flow data for Australia.

I would like to thank all the academic staff at Macquarie University who taught during my undergraduate degree, and provided me with the knowledge and skills that I have put to use in this work, Dr. Craig O'Neill, Dr. Mark Lackie, Dr. Yinjie Yang and many more within the Department of Earth and Planetary Sciences.

Last but not least, this research project would not have been possible without the constant support from my family and friends. To my Mum, Dad and brother, thank you for always believing in me and providing a positive environment for my love of science to grow, I hope I can continue to make you proud. Of course, I am most grateful to my friends, both from University and home, (of which there are too many to name), whose support throughout this year, and also the entirety of my University study, has gotten me over every hurdle and past every stumble I have had, thank you all.

Abstract

The Australian continent is composed of an assemblage of lithospheric blocks that can be broadly grouped into the Precambrian western and central cratonic zones and the Phanerozoic eastern province. The fusion of lithospheric domains, an active accretionary margin, and a sequence of subduction complexes throughout Australia's geological history have created a complex assemblage of lithospheric domains. In this thesis, I map the thermal, physical and compositional structure of this complex lithosphere and sub-lithospheric mantle using a well-developed multi-observable probabilistic inversion method (Afonso et al., 2013a,b). Geophysical observables used in this study include Rayleigh wave dispersion data, absolute elevation, geoid height, surface heat flow, and *a priori* crustal information (e.g. Moho depth, crustal layers, seismic velocity and density). These data sets are jointly inverted using a 1D column-by-column approach with a Bayesian framework, combining prior geophysical knowledge with measured data.

The results from this research include estimates of depth to the lithosphere-asthenosphere boundary, temperature variations and chemical structure in the lithosphere and sub-lithospheric mantle and temperature profiles beneath continental Australia.

Declaration

I certify that the work in this thesis entitled "**A Preliminary Thermochemical Model of the Australian Lithosphere**" has not previously been submitted for a degree, nor has it been submitted as partial requirement for a degree to any other university or institution other than Macquarie University.

I also verify that this thesis is an original piece of research and has been written by me. Any help and assistance that I have received in my research work and the preparation of the thesis itself have been properly acknowledged.

In addition, I certify that all data, information sources and literature used are indicated in the thesis.

Byron Gear

Student ID: 43272487

November 27, 2017

Contents

List of Figures

List of Tables

1

Introduction

1.1 Background and Objectives

The Australian lithosphere (Earth's rigid outermost shell) is composed of three broadly grouped geological provinces; the Precambrian western and central areas, and the Phanerozoic easternmost province (Figure 1.1). For this research it is important to note the geological differences between these regions as they often provide an explanation for geophysical results. While the fusion of cratonic lithospheric domains finalised during the Precambrian, approximately 30% of Australia was added to the eastern accretionary margin during the Paleozoic through a sequence of subduction environments. Archaean lithospheric roots grew beneath Australia concurrently with crustal development via a combination of lateral accretion processes analogous to plate tectonics (e.g. continental collision), and vertical accretion associated with the arrival of mantle plumes (Betts et al., 2002). This created a complex

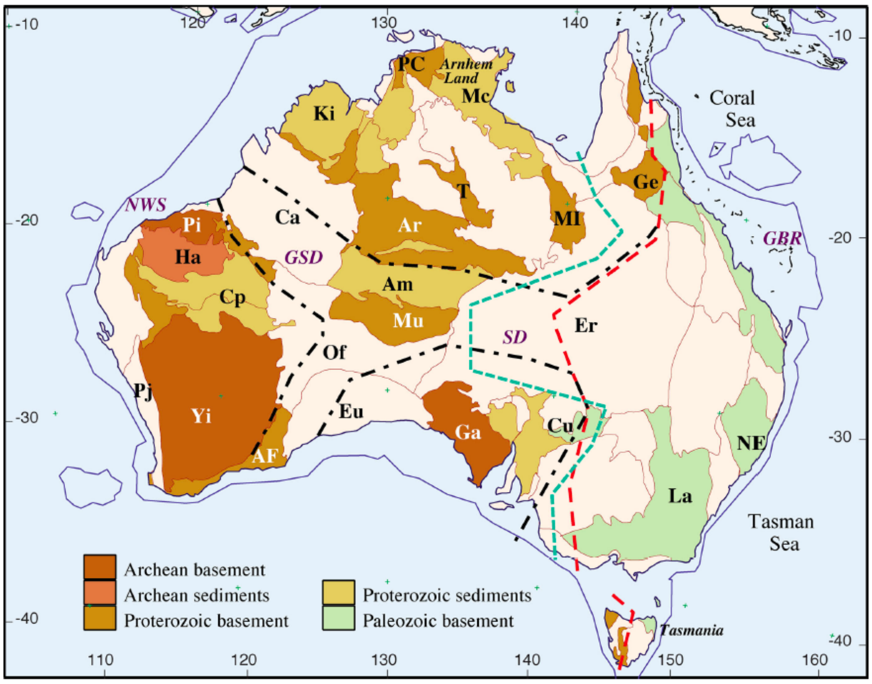

FIGURE 1.1: A representation of the main tectonic features of Australia. The outline of the major cratonic areas is marked by the dotted-dashed lines (West, North and South Australian Cratons). The Tasman Line separating older and younger provinces is shown in red. The cyan dashed line indicates the eastern boundary of the main block of thickened crust. (Kennett et al., 2012)

assemblage of tectonic domains, a simplified representation of the main tectonic features in the study area is shown in Figure 1.1.

The aim of this work is to provide first-order estimates of the complex thermochemical structure of the lithosphere and sub-lithospheric mantle beneath the Australian continent. The thermochemical structure of the upper mantle can give insight into understanding the formation, deformation, growth and destruction of a continent, as well as the interactions between the lithosphere and sub-lithospheric mantle, and the evolution of surface topography. The main data set used in this research is Rayleigh wave dispersion data, as well as geophysical observables including; geoid height, elevation, surface heat flow and *a priori* crustal information (moho depth, crustal layers, seismic velocity and density). The result will be 1D models that can be used to create a pseudo 3D approximation.

These data sets are jointly inverted using a probabilistic inversion technique pioneered and developed by Afonso et al. (2013a,b). This method is designed for high-resolution thermal and compositional mapping of the lithosphere and sub-lithospheric upper mantle and overcomes the problems that accompany traditional inversion techniques (Afonso et al., 2013a). Previous work by Mehdi T. Qashqai (2016) in a Ph.D. research project produced at Macquarie University, used this same probabilistic inversion framework to derive the density and chemical structure beneath; the Western United States, the West Australia Craton and the North China Craton. His work involved further development of the multi-observable probabilistic inversion method (Afonso et al., 2013a,b, 2016b), while this research focuses on providing realistic maps for the continental Australian lithosphere. The methodology used in this thesis follows that of Qashqai's work.

Of course, this is not the first attempt at mapping geophysical properties of the Australian lithosphere, recent models by Khan et al. (2013) provide solutions similar in method and result to that produced here. Khan et al. (2013) employ a probabilistic approach, based on the work of Mosegaard and Tarantola (1995) and Tarantola (2005) to solve the non-linear inverse problem. Their models are parameterised on an unstructured 5° x 5° grid of latitude and longitude, using fundamental-mode and higher-mode surface wave phase velocities. Figure 1.2 shows an example of their results in terms of data they chose to plot at selected depth slices of 100, 150, 200, 250, 300, 350, 400 and 450km . The results from their inversion include mantle compositional variations (e.g. Mg/Fe, Mg/Si), thermochemical modelling (e.g. mantle temperature variations), discontinuity mapping (e.g. moho depth, depth to 410km seismic discontinuity) and mantle shear wave anisotropy variations.

A study by Goes et al. (2005) analysed inverted multi-mode Rayleigh wave dispersion data (Simons et al., 2002; Yoshizawa and Kennett, 2004) to define temperature models (geotherms) in the continental Australian mantle. They converted the shallow mantle S-velocities (80-350km) to temperature resulting in a first order picture of mantle temperatures within the tectonic provinces including Archean, Proterozoic, western and eastern Phanerozoic. This research bares relevance as we also show temperature models in the lithospheric mantle, and will compare results to these models later on.

The Australian Seismic Reference Model (AuSREM) consists of a crustal (Salmon et al., 2012) and mantle (Kennett et al., 2012) component, and is a comprehensive study of the Earth beneath Australia. Ranging from 100°E/10°S to 160°E/45°S the model is based on

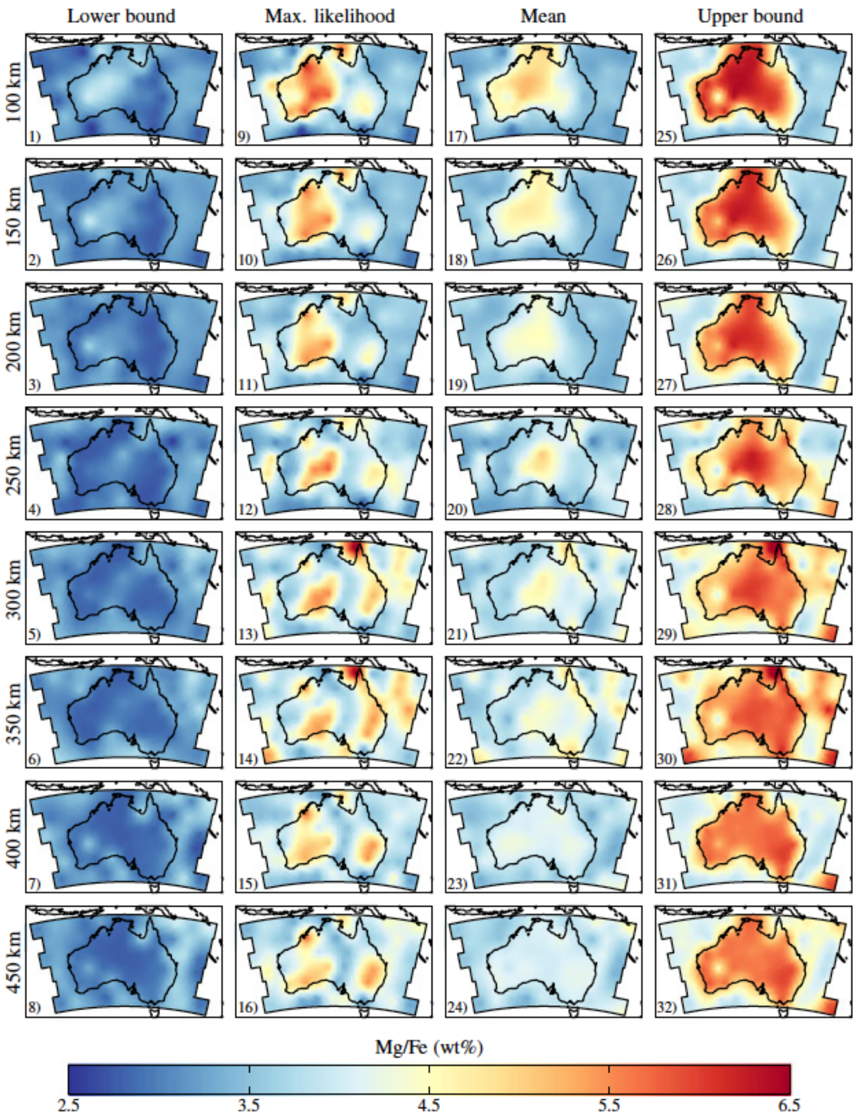

FIGURE 1.2: An example of the models put forward in Khan et al. (2013), showing maps of mantle compositional variations in elemental Mg/Si (wt%) at various depths beneath Australia and surrounding ocean.

a grid with 0.5° sampling in latitude and longitude. The crustal component makes use of all available seismic sources as input data, including reflection/refraction seismics, receiver functions, and tomographic information from ∼15 studies. For the crust they are able to produce sedimentary basin thickness, P and S wave-speed distribution and build on a new map of depth to Moho. The upper mantle component primarily uses surface wave tomography sources, supplemented by body wave arrivals and regional tomography. From this information Kennett et al. (2012) provides models of P and S wave tomography/wave-speeds, density structure, and depth to the Lithosphere-Asthenosphere boundary (LAB). Our models utilise components of the crustal model as initial crustal information, and we compare results from the mantle to models created from this work.

1.2 Thesis Structure

The structure of this work is as follows; introduction, methodology, application to Australia, discussion, conclusions and future work. Section 2 contains a brief explanation of Bayesian inverse theory and multi-observable probabilistic inversion, followed by the forward problems used to invert Rayleigh wave dispersion curves, geoid height, absolute elevation and surface heat flow. It also includes the parameterisation of the crustal layers and the mantle, as well as prior crustal information, e.g. initial models. Section 3 begins to discuss the work in context of Australia, beginning with a geological/geophysical background, then listing the data, pre-processing and inversion method (i.e algorithms and code), and a description of the results. The discussion section details the thermochemical structure of Australia, the crustal and mantle components and the velocity and density structure. Lastly, is the conclusion section which summarises the outcomes from this work and the goals for potential future studies with a full 3-D modelling of Australia.

2 Methodology

2.1 Bayesian Inverse Theory

Applying solutions to geophysical inverse problems provides a means for reconstructing the subsurface structure from a set of geophysical data. The complexity of these problems increases once they become non-linear, and requires the integration of probability and information theory to find a solution (Tarantola and Valette, 1982b). The inverse problem is the opposite of the forward problem, which predicts the results of measurements on the basis of a physical theory within a set of conditions (Menke, 2012). Inverse theory uses mathematical techniques for reducing data to obtain useful information about the physical world. It is important to note that inverse theory does not result in a model, but rather uses observable data in a model, to provide information about the properties of the model parameters.

The data used in inverse theory problems to estimate the model parameters is often not a single numerical value, as this is unrealistic for most experimental data. The results of an experiment are known to contain noise; this causes the data to scatter about the mean value. Hence the data (**d**) is best described by a probability density function (PDF), which uses a random variable, to describe this scattering, and includes information about the range and distribution (Menke, 2012). The assumption underlying Bayesian inverse theory is that each piece of information pertaining to the problem can be described by probability density functions (Tarantola, 2005).

The linear inverse problem is formalised as such:

$$Gm = d \tag{2.1}$$

Where d and m are vectors containing the data and model parameters respectively and G is a linear or non-linear data kernel (depending on the nature of the problem) which links the data and model parameters by a particular physical process. If G is linear then the generalised least squares solution is the most common way to solve an overdetermined (having more data than unknowns in equation 2.1) inverse problem (Menke, 2012; Tarantola and Valette, 1982a; Lines and Treitel, 1984). However, this matrix-based method is ill-equipped to cope with non-linear problems, and so the probabilistic approach to inverse problems combines all available information; data, physical theories and any prior knowledge to define the model parameters.

Since the probabilistic nature of Bayesian theory has the power to provide uncertainty values associated with model parameters, the results of measurements is now a *state of information* that includes said uncertainties acquired for observable data (Tarantola, 2005). The state of information in the data space and the model space can now be represented by probability densities $\rho(d)$ and $\rho(m)$ respectively, such that $\rho(d, m)$ can represent a *joint* prior probability density for prior information obtained on the data and model parameters (Tarantola, 2005). The general solution to the inverse problem is therefore an *a posteriori state of knowledge* which represents all the information about the problem. The solution within the geophysical literature was first formulated by Tarantola and Valette (1982b):

$$\sigma(d, m) = k\frac{\rho(d, m)\Theta(d, m)}{\mu(d, m)} \tag{2.2}$$

where $\sigma(d,m)$ represents the *a posteriori state of knowledge*, k a normalisation constant, $\Theta(d,m)$ is the probability density associated with the physical theory connecting the model parameters and the data, and $\mu(d,m)$ is the homogeneous PDF.

The true power of Bayesian inversion lies in the fact that the posterior distribution is largely reliant upon the quality of the *a priori* information provided. With this comes the freedom to use the a priori model statistics as a way to adjust/control the properties of the outputted model (Scales and Snieder, 1997). Considering the equation for the posterior information in the model space:

$$\sigma(m) = k\rho(m)L(m) \tag{2.3}$$

where k is a normalisation constant and $L(m)$ is referred to as the *likelihood function*. This aptly named function gives a measure of how well a particular model explains the data (Afonso et al., 2013a; Qashqai, 2016). Figure 2.1 shows a system with only one model parameter, if then, the observed data are extremely sensitive to this parameter and the physical theory describing the problem is exact, the likelihood function will be tight with the true value of the parameter as will the PDF of the model space (Figures 2.1a and 2.1b). The quality of the a priori information is quite poor here and yet it does not have a considerable control over the posterior PDF (Afonso et al., 2013a). Figures 2.1c and 2.1d show a contrary situation where the data is insensitive to the model parameter, then the a priori information strongly determines the quality of the posterior PDF.

2.2 Multi-observable Probabilistic Inversion

In recent years an adaptive method of Bayesian inverse theory has been developed, whose key aspect is the ability to combine multiple observables into a single thermodynamic-geophysical framework. The method is known as multi-observable probabilistic inversion, developed in majority within the last 10 years, it's designed to be particularly suited for this sort of research, involving thermal and compositional mapping of the lithosphere. The following section is a summary of this methodology as described in Afonso et al. (2013b) in the context of our work (that is, with alternate algorithms and numerical value setting). The method is

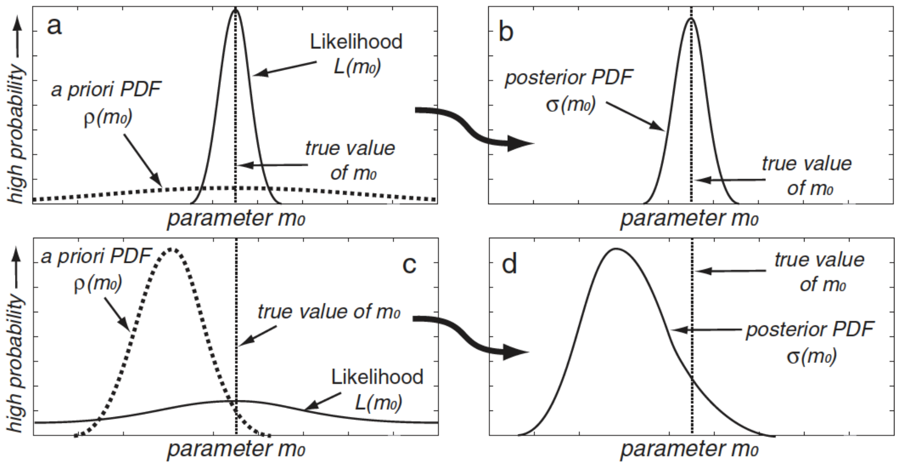

FIGURE 2.1: The relationship between posterior PDF and $L(m_0)$ and $\rho(m_0)$. **a and b** The posterior PDF is controlled by $L(m_0)$ as prior information is poor, and it offers a good estimate of the true value. **c and d** The posterior PDF is controlled by faulted prior information and so the posterior PDF is skewed towards highly probable wrong values (Afonso et al., 2013a).

used for this research as a alternative to traditional (i.e. non-probabilistic) inversion methods which are not equipped to deal with the strong non-linearity of the system (among other problems, see Afonso et al. (2013a) and Afonso et al. (2013b)).

The full usage of this method is capable of producing 3D high-resolution maps of the thermochemical subsurface structure. Figure 2.2 shows the two stage system for the inversion method, which was subdivided by Afonso et al. (2013b) in this way to make the problem easier to deal with. However, our methods only utilise the 1D component (first part) of the method, as the full 3D problem is more time consuming and suited to a Ph.D. length research project. The inputs include the main dataset and initial models that will be discussed in greater detail in Section 3. The main processing involves the inversion of 1D columns by means of the Monte Carlo sampling method, with an emphasis on temperature and composition respectively. The result is a 1D data PDF for each column that would be used as *a priori* information in a Bayesian formulation in the second stage for 3D refinement.

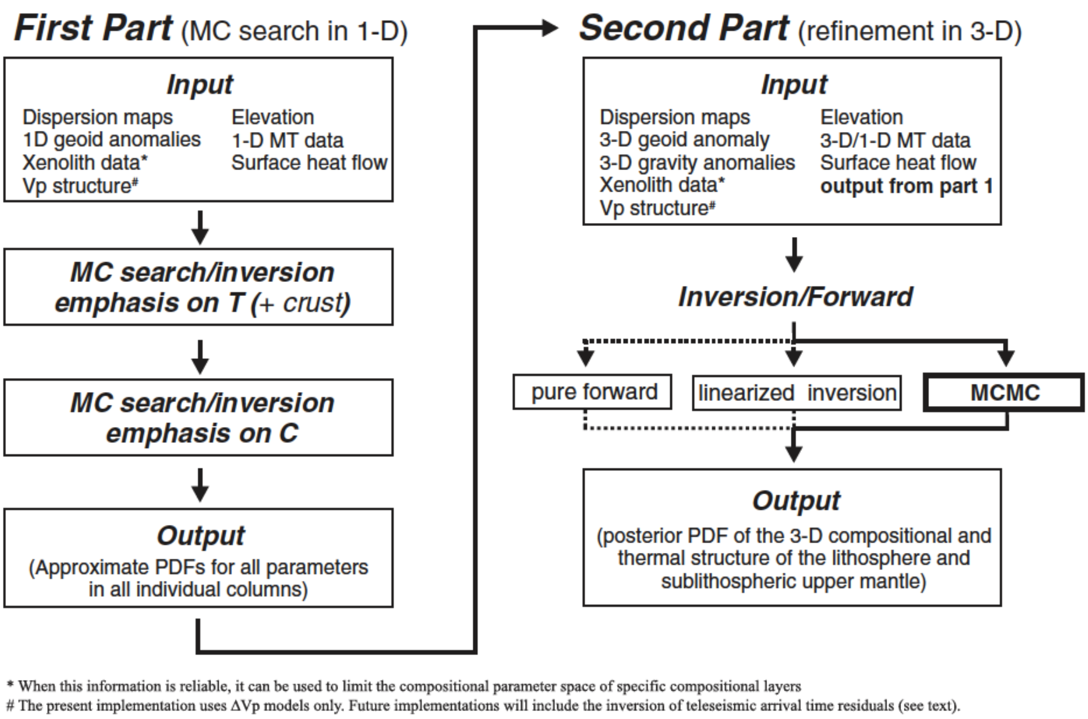

Figure 2.2: Flow chart showing the two part inversion process layed out by Afonso et al. (2013b). 'MC' refers to Monte Carlo, while Markov Chain Monte Carlo is abbreviated to 'MCMC', 'T' = Temperature, 'C' = Composition, 'MT' = Magnetotelluric, 'PDF' = Probability density function.

2.2.1 Column by Column Inversion

Given the non-linearity of the system and the high number of free parameters, a probabilistic Monte Carlo sampling approach is used to solve the inverse problem for each individual column. While Afonso et al. (2013b) utilises a modified version of the Neighbourhood Algorithm (NA) (Malcolm, 1999), we use an efficient combination of algorithms known as Delayed Rejection Adaptive Metropolis (DRAM) (Haario et al., 2001, 2006; Qashqai, 2016). A summary of the two algorithms involved their combination is given in section 3.3.1 of this work, with full details given in Haario et al. (2001) and Haario et al. (2006). This search process must be repeated for each column of which there are approximately 250 in our region of interest, with each column being 2°x2°.

Observations (data) can have different sensitivities to changes in model parameters, and not recognising this and accounting for it in the system can lead to incorrect true values of model parameters (Afonso et al., 2013a) . For instance, variations in temperature have been found to be the main parameter affecting geophysical observables, more so than changes in bulk composition. Afonso et al. (2013a) solve this problem by subdividing 1D sampling stage into two parts, temperature and composition, however we use an updated version of this method which no longer separates these two steps and they are now together in one single step.

2.3 Forward Problems

The forward problem in this thesis is almost a clone of that used in Qashqai (2016) and includes: a) numerical solution of the 1D steady-state heat conduction equation, b) calculation of physical properties (i.e seismic velocities and density) in the upper mantle using Gibbs free-energy minimisation, c) solving isostatic balance to predict surface elevation, d) computing geoid height, e) computing the fundamental mode of Rayleigh wave dispersion curves. These problems are solved in every simulation, when model parameters are sampled from their proposed PDFs.

2.3.1 1D Heat Conduction Equation

Fourier's law of heat conduction gives the rate of heat flow per unit area (Q) through a material, expressed in one dimension as:

$$Q(z) = -k\frac{dT}{dz} \tag{2.4}$$

where k is the thermal conductivity constant and $\frac{dT}{dz}$ is the temperature gradient. Given a steady-state, where there is no temperature change with time, the heat equation for any material in the Earth's lithosphere is given by:

$$\frac{d^2T}{d^2z} = -\frac{H}{k} \tag{2.5}$$

where H is radiogenic heat production.

The crustal and lithospheric geotherms are then calculated by computing the steady-state heat conduction equation using the finite difference method, which are subject to the following Dirichlet boundary conditions: $T = 10°C$ at the surface of the Earth and $T = 1250°C$ at the base of the thermal lithosphere (Qashqai, 2016).

2.3.2 Gibbs Free-energy Minimisation

Mantle mineral assemblages and physical properties V_p, V_s and ρ, are computed using components of the thermodynamic code `Perple_X`, within the system of CFMAS ($CaO - FeO - MgO - Al_2O_3 - SiO_2$). `Perple_X` was developed by Connolly (2005) to compute these properties by Gibbs free-energy minimisation as a function of composition, pressure and temperature, also utilised in forward problems by Qashqai (2016); Khan et al. (2013); Afonso et al. (2013b). The details of this software are described in Connolly (2005).

Temperature, pressure and composition are required to compute the mineral assemblages at each depth node. Temperature values that are acquired by solving the heat conduction equation in the previous sub-section are used to obtain temperatures in the lithospheric mantle (via interpolation). With pressures in the upper mantle computed using a quadratic equation that is dependent on the depth at each node (Qashqai, 2016).

2.3.3 Isostatic Balance

Lithospheric isostasy is the application of hydrostatic equilibrium to the Earth's lithosphere. In this work the large majority of data columns are continental (above sea-level) however there are a number of columns that are on the continental shelf or even abyssal plane (below sea-level) and as such we present the equations related to both cases. Following Afonso et al. (2008) we take a reference column to be at a mid-oceanic ridge (MOR) (Figure 2.3), in order to calculate absolute elevation. A calibration with respect to a reference column at a MOR is chosen as this is where average elevations, petrogenetic processes and lithospheric structures are known in greater detail than anywhere else on Earth. Here elevation above (E_a) and below (E_b) sea-level are given respectively by:

$$E_a = \int_{L_{top}}^{L_{bottom}} \frac{\rho_b - \rho_l(z)}{\rho_b} dz - \Pi \tag{2.6}$$

$$E_b = E_a \frac{\rho_b}{\rho_b - \rho_w} \tag{2.7}$$

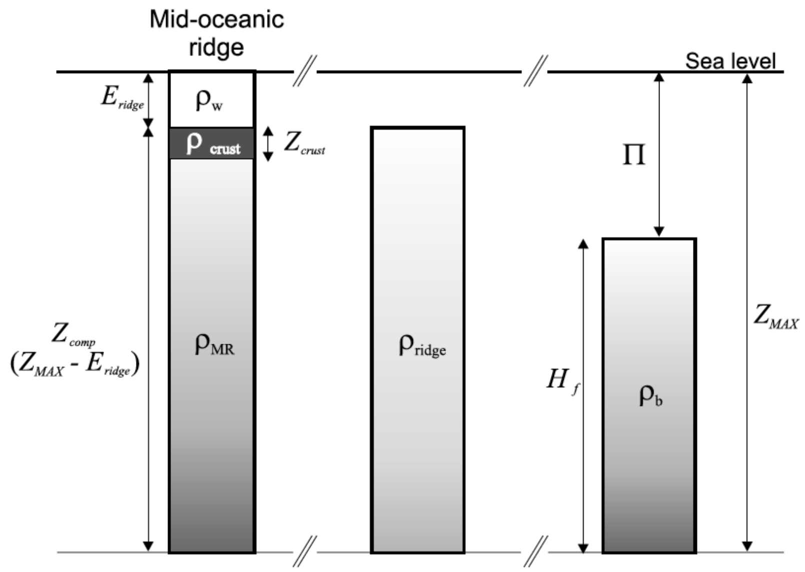

FIGURE 2.3: Isostatic balance used to calculate the absolute elevation of different columns with respect to a reference column at a MOR (Afonso et al., 2008).

where L_{top} is taken from at the top of the column, L_{bottom} is taken at the bottom of the column, ρ_b is the density of the mantle at 400 km depth, $\rho_l(z)$ is the depth-dependent density, ρ_w is the density of seawater and Π is a calibration constant which is dependent on the reference column. The reader is referred to Afonso et al. (2008) for more details.

2.3.4 Geoid Height

Since not all density anomalies in our models are isostatically compensated within the lithosphere we solve the gravity potential equation for a cylinder (1D column approximation) for sub-lithospheric density distributions, given by:

$$\Delta N = \frac{2\pi G}{g_0} \int_0^H \Delta\rho(z)[(R^2 + z^2)^{\frac{1}{2}} - z]dz \tag{2.8}$$

with radius $R = \sqrt{V/\pi h}$ where h and V are the height and the volume of the cylinder, respectively. In Eq. 2.8, H is the total thickness of the model, G the universal gravitational constant, $\Delta\rho$ refers to the density difference between a problem column and a reference density column, and g_0 the reference acceleration of gravity on the reference geoid. The equation is then numerically integrated using the finite difference mesh where the interval between successive nodes is 2km. For density anomalies within the lithosphere, Eq. 2.8 is solved in its "isostatic" form (see Afonso et al. (2016b)), which is independent of R. For density anomalies at sub-lithospheric depths, Eq. 2.8 needs to be solved with consideration of R.

The radius of the cylinder given by parameter R is unbounded in Eq. 2.8. As discussed in Afonso et al. (2013b) and Qashqai (2016), 3D volume can be discretised into 1D columns, hence the value of R must be chosen such that it guarantees the 1D assumption is a good first-order approximation of the real 3D effects (Afonso et al., 2013b). Unfortunately there is no simple rule to determine the value of R, however, in practice it is relatively straightforward to obtain proper values by running synthetic tests (Qashqai, 2016). Values of R that are too low underestimate the effects of shallow density anomalies compared to their real 3D signature. Similarly, much larger values of R would overestimate the effect of deep density anomalies (Afonso et al., 2013b), a radius of 80km is used in this work.

2.3.5 Rayleigh Wave Dispersion Curves

Rayleigh waves are used in this work, and the dispersion curves are calculated using a modified version of the program *disp*96 (Herrmann, 2013). Following Qashqai (2016) the code starts the computation of dispersion curves for fundamental mode by choosing an initial small value of phase velocity. For the selected value of phase velocity, it computes quantities needed for constructing a matrix associated with each layer in a loop from the first to the n-1 layer. The Thompson-Haskell matrix is then formed by multiplication of matrices. Following this, a root-search algorithm is used to search for non-trivial solutions of the matrix. The value of the found phase velocity is then used as the starting value for the next frequency, etc.

2.4 Model Parameterisation

It is important to note the parametrisation of the model and the numerical discretisation scale used to solve the forward problem of each 1D column. In this thesis, the model is defined by three crustal layers; sedimentary, upper and lower, as well as two upper mantle layers; lithospheric and sub-lithospheric.

Each crustal layer is characterised by its own set of physical parameters including coefficient of thermal expansion (α), compressibility (β), thermal conductivity (k), bulk density at surface P-T conditions (ρ_0), V_p/V_s and thickness (h). Additionally, only one parameter is used for the average radiogenic heat production (RHP) within the crust. Previous studies by Shan et al. (2014) and Afonso et al. (2016b) have shown that results from forward problems are mainly controlled by variations in the last 4 parameters, hence they are treated as unknowns in the inversion, while the first three (α, β, k) are kept as constants. Lithospheric and sub-lithospheric layers are defined by five major oxides in the CFMAS system ($CaO - FeO - MgO - Al_2O_3 - SiO_2$) and their sum is constrained to 100%. According to this constrain, in each compositional layer, only four of them ($CaO - FeO - MgO - Al_2O_3$) are treated as unknown parameters (Qashqai, 2016).

Three discretisation scales are used to solve the forward problems, with the finest discretisation represented by the finite-difference mesh used to solve forward problems related to geoid height, isostasy, and 1D heat transfer. These are known as *computation nodes*, of which there are 204 in our models, at intervals of 2km. The next, intermediate mesh is constructed in the upper mantle, and consists of 16 *thermodynamic nodes* (15 in the lithosphere and 1 in the sub-lithosphere) used in the solution of the Gibbs free-energy minimisation problem. The coarsest discretisation scale is represented by the compositional layers of which there are two; in the lithosphere and sub-lithosphere respectively.

The Lithosphere-Asthenosphere boundary (LAB) is thermally defined in our parameterisation as the 1250°C isotherm (T_{1250}), with the transition from conductive lithosphere to convective asthenosphere modelled as a thermal buffer of constant thickness 40km. In this transitional layer, heat transfer is controlled by both conduction and convection and the temperature at the base (T_{buffer}) is allowed to vary during the inversion. Below this transitional layer, two additional free parameters for temperature are introduced: one at the bottom of the model (T_{bottom}), and the other (T_{inter}) at a node depth between the T_{buffer} and T_{bottom}, coinciding with one of the intermediate nodes in the sub-lithospheric mantle. The 1D temperature structure within the sub-lithospheric mantle is then obtained by linear interpolation of these four temperatures.

2.5 Prior Information

A priori information is defined as any information that is independent of measurements and results; it can be applied to model parameters (m) and observable parameters (d). Prior information on m refers to any idea or prejudice about potential distributions for models, and when on d it may relate to uncertainties on actual measurements and datasets.

2.5.1 Compositional Parameters

The atomic ratios of the five main oxides, $SiO_2 - Al_2O_3 - MgO - FeO - CaO$ have been found to be related to some geophysical observables. An important ratio is between MgO and FeO, known as the magnesium number, Mg#. There have been clear correlations between Mg# of a residue and its bulk density, shear and compressional velocities and electrical conductivity (Afonso et al., 2010, 2013a). Al_2O_3 is another important compositional indicator, the oxide has a strong influence on bulk density and seismic velocities of peridotites.

The Markov Chain Monte Carlo method used in this thesis involves generating many random compositional samples within the system of oxides $CaO - FeO - MgO - Al_2O_3 - SiO_2$. One method for generating, statistically independent and representative, samples is given by Afonso et al. (2013a) and consists of the following steps:

1. Choose a wide initial variation range for Al_2O_3 and FeO that covers >95% of the entire natural variability, and assign a uniform probability density within these ranges (i.e., equal probability to all values within the chosen range).

2. Select a value for Al_2O_3 and FeO within their respective variation ranges using a random sampler.

3. Use the selected Al_2O_3 value with the $Al_2O_3 - MgO$ and $Al_2O_3 - CaO$ regressions to obtain a preliminary (mean) value for MgO and CaO.

4. Randomly select a new value for MgO and CaO from the known probability distributions associated with each Al_2O_3 value. Typically, we will use a Gaussian distribution.

5. Calculate the SiO_2 content of the present sample as 100-$(FeO+CaO+MgO+Al_2O_3)$.

2.5.2 Crustal Information

In our model, initial values for the crustal thickness variations in the sedimentary layer are provided by CRUST1.0 (Laske et al., 2013). However, these thicknesses are given a range of variability bounded by maximum and minimum values defined by us during the inversion, hence our results are largely independent on the quality of this initial crustal model. The prior values for crustal parameters (V_s, V_p, ρ), including moho depth, are provided by the Australian Seismological Reference Model (AuSREM) (Salmon et al., 2012). While the first crustal layer is defined by the values in CRUST1.0, the next two layers are determined by dividing the remaining depth to the moho in two (unless significant discontinuities are shown in the AuSREM crustal component).

3

Application to Australia

3.1 Geological and Geophysical Background

Australia is known for its complex tectonic provinces and lithospheric structure, which are commonly grouped into; Archaean, Proterozoic and Phanerozoic provinces. Each shaped by the complex evolution of crustal development and lithospheric growth. The following section gives an outline of the geological history and significance of each area based mainly on the comprehensive study of Betts et al. (2002).

3.1.1 Archaean Province

The majority of Archaean provinces (e.g. Pilbara and Yilgarn Cratons) exist in what is termed the West Australian Craton, while the Gawler Craton, which is also of Archaean age, lies in the South Australian Craton (Figure 1.1). The Pilbara Craton has a tectonic history between 3.65 and 2.0 Ga. This region consists of overlaying packages of volcano-sedimentary (greenstone) units, metamorphosed komatiite, dacite, tholeiitic basalt and calc-alkaline volcanics. Uniquely formed domes of granite-greenstone belts in the central and eastern Pilbara have two competing theories for development, a 'convective overturn' (Collins et al., 1998) and 'metamorphic core complex' (Zegers et al., 1996) model. Betts et al. (2002) puts forward a compromise that evidence of the early stages of 'convective overturn' may be indistinguishable from evidence for a 'metamorphic core complex'.

The Yilgarn Craton is composed in majority of low metamorphic grade granite-greenstone rocks that formed between 3.73 and 2.55Ga. Low-angle thrusts, isoclinal and sheath folds started a process of north-south shortening in the Yilgarn which evolved into east-west shortening forming thrusting and upright faulting (Chen et al., 2001). Dating of zircons in the Yilgarn and Gawler Cratons suggests that the regions grew from continental crust as old as 4.3 and 3.15Ga respectively.

Lithospheric growth in the Archaean is thought to be a joint effort of vertical and horizontal processes (Myers, 1993; Collins et al., 1998). Evidence exists to support both mantle plume activity being a method for cooling the interior of the Earth and plate tectonics (subduction, crustal accretion) being a mechanism of heat loss at the surface.

3.1.2 Proterozoic Lithospheric Growth

The Proterozoic was a highly tectonically active period in the evolution of the Australian continent, abundant in orogenic events resulting from continent-continent collisions and accretionary belts. Continent-continent collision of Kimberley and North Australian Cartons during the Halls Creek Orogeny (1.82Ga) was followed by the Barramundi orogenic event which itself began a period of crustal shortening (Tyler and Griffin, 1990; Etheridge et al., 1987). In addition to this a long-lived accretionary margin with a subduction system along the southern margin of the North Australian Craton occurred concurrently with a continental backarc basin in the continent interior. This basin development was interrupted by a series of Mesoproterozoic orogenic belts along the eastern margin of the Australian proterozoic continent. Several more orogenic events took place after this including the Grenville-aged orogenic belt (where the South and North Australian Cratons were reattached) and the Petermann Ranges orogeny (when deformation along fault planes and partial melting resulted in localised inversion of the Centralian Superbasin).

The complex evolution of the Proterozoic crust involving multiple episodes of continental collision and accretion with periods of basin development in-between, understandably translates to complexities and an amount of speculation when determining the structure of the Proterozoic lithosphere. Betts et al. (2002) goes into some detail about the supporting and refuting theories for Archaean lithospheric roots under Proterozoic crust, but ultimately dismisses the idea as unequivocal and speculative. However there is some grounds to support crustal thickening as it's indicative of significant lithospheric thickening and areas with prolonged extensional tectonism during the Palaeoproterozoic should have resulted in the thinning of any existing lithospheric root. While areas that did not undergo significant crustal extension are characterised by a relatively thin crust and lithosphere (e.g. the Kimberley Craton).

3.1.3 Phanerozoic Continental Growth

From 800-600Ma continental rifting formed a passive margin along the eastern margin of continental Australia, continuing into the Middle Cambrian. The Paleozoic evolution of continental growth is marked by two major orgenic belts; the Lachlan and New England Orogens. Between the Cambrian and late Permian these two orogenies involved episodic backarc development, accretionary collisional events and backarc inversion, with evidence suggesting that the orogenies evolved simultaneously (Leitch and Cawood, 1987). It is interesting to note that over this ∼500 million year period they evolved without any continent-continent collision, and the well-known eastward accretion caused the continent to grow by 30% (Gray and Foster, 1998).

3.2 Data and Processing

The geographical extent of the area modelled lies between 10°S and 44°S in latitude, and 112°E and 154°E in longitude (Figure 2.3). The area is subdivided into a 2°x2° grid. At each of these grid points is a 1D column of data used in the inversion process (section 2.2.1), the data include geoid height, absolute elevation, surface heat flow (all with relative uncertainties), intial crustal information (V_s, V_p, ρ,moho depth) and the main data set of surface waves. It is important to note that the figures we provide here have a much higher resolution than 2°x2° as we have re-sampled the data to a higher resolution in post-processing. Not all columns are used in the inversion, as one can see from Figure 3.1, roughly a third of the area is located over oceanic crust, which is of no use in our study, nor is the prior crustal information accurate in these areas. Approximately 250 columns of the 357 in total were active in the final inversion. The following section defines the individual sources and methods of acquisition of each data set.

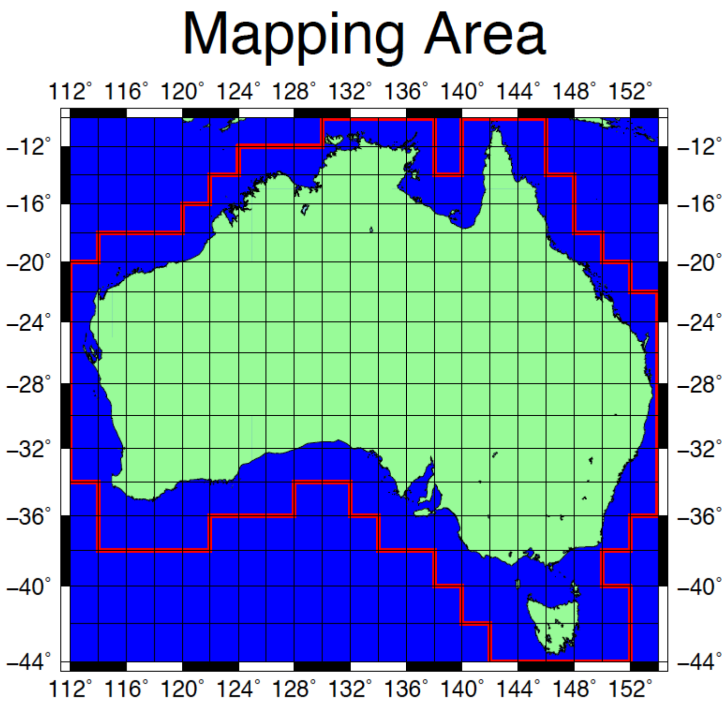

FIGURE 3.1: The mapping area with grid lines at increments of 2°. Columns within the red polygon are those active for the inversion process.

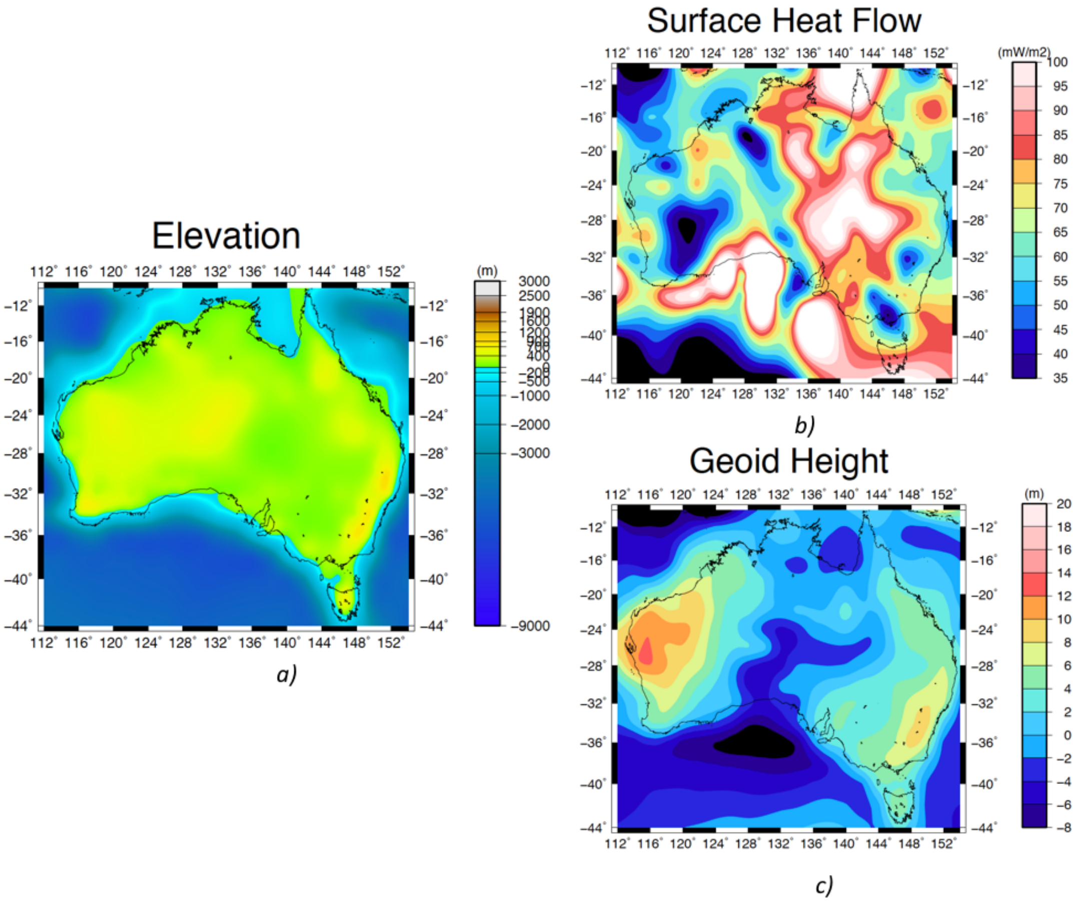

Figure 3.2: Maps of the input elevation (a), surface heat flow (b) and geoid (c) used in the inversion process

3.2.1 Geiod Height, Elevation and Surface Heat Flow Data

The global Earth model EGM2008 (Pavlis et al., 2012) was used to extract the average geoid height (Figure 3.2c) at the centre of each grid interval, the model contains spherical harmonic coefficients up to degree 2190. During a pre-processing stage the total geoid was filtered to remove the effects of density anomalies deeper than approximately 400km. Uncertainties for elevation, geoid height and surface heat flow were computed as follows: we read all available data points within a prescribed cell and compute the mean and variance of all values within that cell. During the joint inversion, each cell is assigned a mean and variance. Note that these are not true observational uncertainties, but rather a measure of the natural variability of the fields within each columns surface. We assigned a minimum uncertainty of 1.5m for the geoid height of each cell. The latter uncertainty value is not only associated with an observational component, but it includes a modelling component as well. The input values for elevation (Figure 3.2a) were estimated using ETOPO1 global relief model (Amante and Eakins, 2009), with a minimum uncertainty of 150m assigned. The average surface heat flow values (Figure 3.2c) were extracted from a dataset provided by Derrick Hasterok, Department of Earth Sciences, University of Adelaide, Australia. The data came with a warning to ignore heat flow data over the oceanic crust as most of it is affected by hydrothermal circulation. Again the uncertainties were given a minimum value of 15% of the heat flow value.

3.2.2 Rayleigh Wave Dispersion Data

For this research only fundamental-mode Rayleigh dispersion curves were extracted from a dataset generously provided by Kazunori Yoshizawa, Earth and Planetary Dynamics, Hokkaido University, Sapporo, Japan (Figure 3.2)(Yoshizawa, 2014). Yoshizawa (2014) acquired this data using three-component broad-band seismograms of the FDSN stations from 1990 to 2007 provided by IRIS Data Management Centre, as well as those of the portable seismic stations in Australia in the period from 1993 to 2004. Seismic events with moment magnitude between 5.0 and 7.5 are used in the waveform analysis. More than 8000 paths were gathered for the fundamental mode Rayleigh waves for the majority of their target frequency range (less than 30 mHz).

While the data is of high quality the standard error is generally underestimated and the values provided in Yoshizawa's data set were ignored. Instead, general uncertainties for similar areas are used, typical values of $\sim$10m/s at 10s to $\sim$80m/s at 140s are given in Guo et al. (2016) and extrapolated to $\sim$100m/s at 250s in this work.

3.3 Inversion Method

We use a probabilistic framework to solve the inverse problem and produce posterior PDFs for all parameters in all individual columns. This is done using a multi-observable probabilistic inversion as described in section 2.2 and Afonso et al. (2013a,b). The posterior PDF is

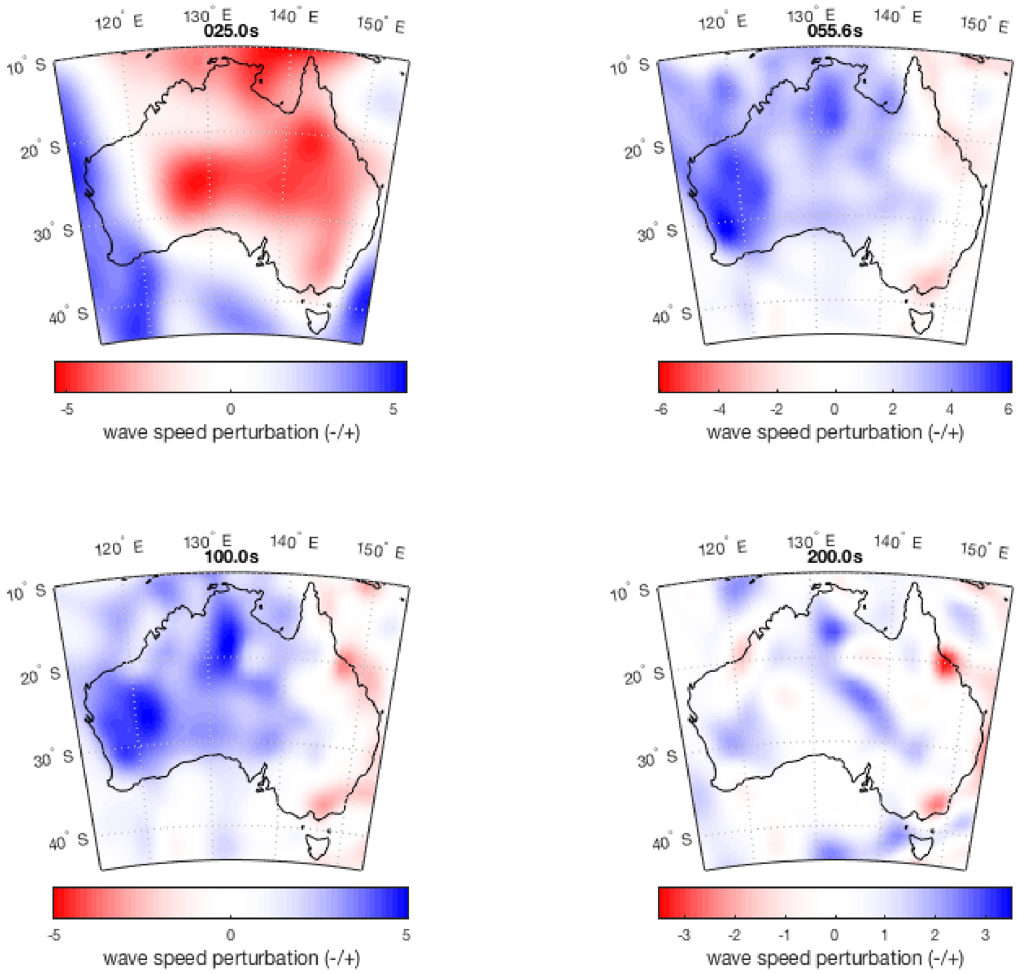

Figure 3.3: Examples of dispersion maps for fundamental-mode Rayleigh waves at 25s, 55.6s, 100s and 200s period.

then sampled using a Monte Carlo Markov Chain (MCMC) sampling approach with an efficient algorithm, known as Delayed Rejection Adaptive Metropolis (DRAM) (Haario et al., 2006), also utilised in the methodology of Qashqai (2016). This is a combination of the Delayed Rejection (Mira, 2001) and Adaptive Metropolis (Haario et al., 2001) algorithms. The inversion software used in this work is `LitMod1D_4INV`, version 2.0, created by J.C. Afonso at Macquarie University in January 2016, with collaborators; J. Fullea, J. Connolly and M. T. Qashqai.

3.3.1 Delayed Rejection Adaptive Metropolis (DRAM)

The main algorithm is still based on the well-known, two-stage, Metropolis-Hastings (MH) (Metropolis et al., 1953) algorithm. The first stage randomly samples only one proposal distribution at each simulation for the model, which depends on the current state of the chain. The second stage is to accept or reject the sampled model. This method of accepting or rejecting one model at a time and moving forward can cause most of the models to be rejected should the variance of the proposed distribution be too high (Qashqai, 2016). Applying the delayed rejection (DR) algorithm provides a way of rectifying these issues with inappropriate proposals. Once a sample is proposed and rejected by the MH rule, instead of retaining the current state and advancing, delayed rejection allows for another sample from a different distribution. By this method the sampling rate is improved by reducing the number of rejected models.

The choice of the proposal distribution from which the new model parameters are drawn can be arbitrary in the MH algorithm. In the cases where the proposal variance is selected to be very small, regions with medium to high probability are sampled from the proposed distribution which may be inappropriately chosen. A solution can be provided by the adaptive metropolis (AM) algorithm, which adapts the MH proposal distribution using the history of the whole chain. The covariance of the proposal distribution is adapted using all accepted models so far to avoid sampling regions with low probability in the posterior PDF.

The combination of these two algorithms into a single DRAM algorithm allows for the most efficient sampling of the parameter space. Following Qashqai (2016) the algorithm has a non-adapting initial stage where model parameters are sampled by the DR algorithm from their initial prior PDFs which are uniform distributions (Table 3.1). In the next stage a multivariate Gaussian distribution (constructed from all previous samples in the chain) is proposed to randomly draw a new model, updated several times at regular intervals during the inversion. In our inversion we use 160,000 samples in the initial stage, with 3 adaptations. The total number of samples tested during the inversion (per column) is 160,000.

Parameters	**Minimum bound**	**Maximum bound**
LAB (km)	55	330
Al_2O_3 in the lithospheric mantle (wt%)	0.5	4
FeO in the lithospheric mantle (wt%)	6	9.2
MgO in the lithospheric mantle (wt%)	34	55
CaO in the lithospheric mantle (wt%)	0.1	5.5
Al_2O_3 in the sub-lithospheric mantle (wt%)	2	4.5
FeO in the sub-lithospheric mantle (wt%)	6	9.2
MgO in the sub-lithospheric mantle (wt%)	34	55
CaO in the sub-lithospheric mantle (wt%)	0.1	5.5
T_{buffer} (°C)	1230	1500
T_{int} (°C)	1230	1650
T_{410} (°C)	1330	1650
STP density (first crustal layer) (kg/m^3)	2000	2750
STP density (second crustal layer) (kg/m^3)	2400	2850
STP density (third crustal layer) (kg/m^3)	2650	3150
V_p/V_s *(first crustal layer)*	1.65	2.2
V_p/V_s *(second crustal layer)*	1.65	1.9
V_p/V_s *(third crustal layer)*	1.65	1.9
Δh *(first crustal layer)* (km)	-2.5	2.5
Δh *(second crustal layer)* (km)	-5	5
Δh *(third crustal layer)* (km)	-5	5
RHP $(\mu W m^{-3})$	0.4	1.8

Table 3.1: All unknown parameters and prior ranges used in the inversion. RHP = radioactive heat production, STP = standard temperature and pressure.

3.4 Description of Results

3.4.1 Fit to Data

Figure 3.4 shows maps for observed and predicted elevation, geoid height and surface heat flow. Elevation and geoid height are well fitted; in most cases predictions are within 1 standard deviation of the natural variability of the fields. Predicted surface heat flow follows the spatial distribution of the observed anomalies, but the amplitudes are smaller than those in the data. This is likely a consequence of having used relatively low upper limits for the average radioactive heat production (RHP) in the crust (see Table 3.1). The Australian crust is known to have some extremely high RHP ($\sim 3 \mu W m^{-3}$ in Paleozoic provinces) in some regions at shallow depths (Sawka and Chappell, 1986; Eppelbaum et al., 2014). We have not allowed for such high values in our inversion and consequently we are not able to reproduce the actual amplitudes of the maximum anomalies. We discuss this further in Section 4.1.

Figure 3.5 shows that observed dispersion values (blue circles) are well fitted by the calculated dispersion curves (red lines).

3.4.2 The Depth to LAB and Thermal Structure

The depth to the thermal (1250 °C isotherm) Lithosphere-Asthenospere boundary (LAB) is shown in Figure 3.6. This figure shows a thick lithosphere beneath the Archaean Yilgarn, Gawler and Pilbara cratons (∼280km), and a much thinner (∼100km) Phanerozoic eastern Australia. This pattern is in agreement with previous estimates using different methods (Kennett et al., 2012; Yoshizawa, 2014), although our estimates are slightly deeper in the deepest LAB regions compared to those in e.g. Kennett et al. (2012). We are cautious about our deepest values as we have assumed a single attenuation model for the entire region (See Afonso et al. (2016b) for details on the attenuation model). However, there is evidence that some regions in Australia (particularly, those coinciding with thick lithosphere) are characterised by very low attenuation values. We discuss this further in section 4.4. The standard deviation represented in Figure 3.6 shows a variability of 16-24km for the majority

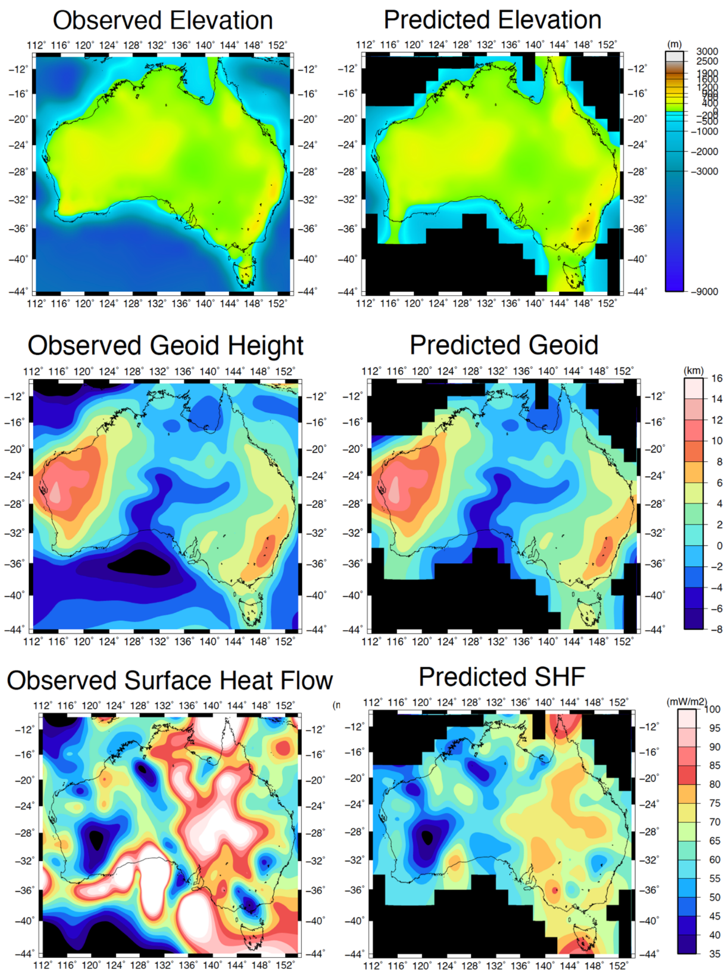

Figure 3.4: A comparison of observed (left) and predicted (right) values for elevation, geoid height and surface heat flow.

of Australia with even lower values on the east coast, this equates to ∼ 10% uncertainty or less.

Figure 3.7 shows temperature variations at depths within the lithosphere (50, 150, 250km) and sub-lithospheric upper mantle (350km). There are clear correlations between LAB depth and thermal structure, most evident at 150 and 250km depth intervals. At these depths cold regions in the West and North Australian cratons correspond to the thickest parts of the lithosphere in our model. This correlation extends to tectonic provinces in the crust, as older Precambrian provinces (e.g. Yilgarn craton) appear to be underlain by lithosphere that is much thicker and colder when compared to Proterozoic regions east of the Tasman line. A closer look at the temperature profiles for the major craton groups (Figure 3.8) confirms some

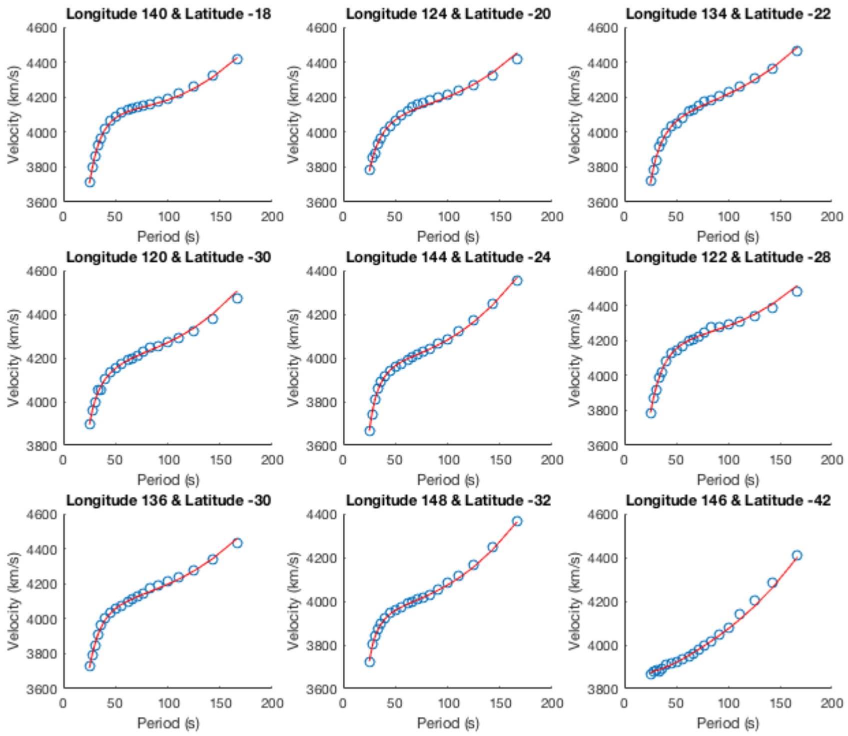

FIGURE 3.5: Examples of calculated dispersion curves (lines) with the fit to observed data (circles).

of these assumptions, with the North and West Australian Cratons showing comparatively cold temperatures to the South Craton and easternmost edge of the continent. Differences in temperature between these regions can reach ∼500°C.

3.4.3 The Compositional Structure of the Mantle

Figures 3.9, 3.10 and 3.11 show that the lithosphere is compositionally distinguishable from the sub-lithospheric upper mantle. The magnesium number (Mg#) has been briefly mentioned above in section 2.5.1, and is calculated using MgO and FeO [$Mg\# = \frac{MgO}{MgO+FeO}\times 100$]. This parameter is known to be a good indicator of the degree of depletion or fertilisation of mantle peridotites, especially when used in conjunction with Al_2O_3 (Figure 3.10) and CaO (Figure 3.11) concentrations. Figure 3.9 shows that areas known to be Archaean cratonic regions, are generally characterised by high Mg# and impoverished in Al_2O_3 and CaO within

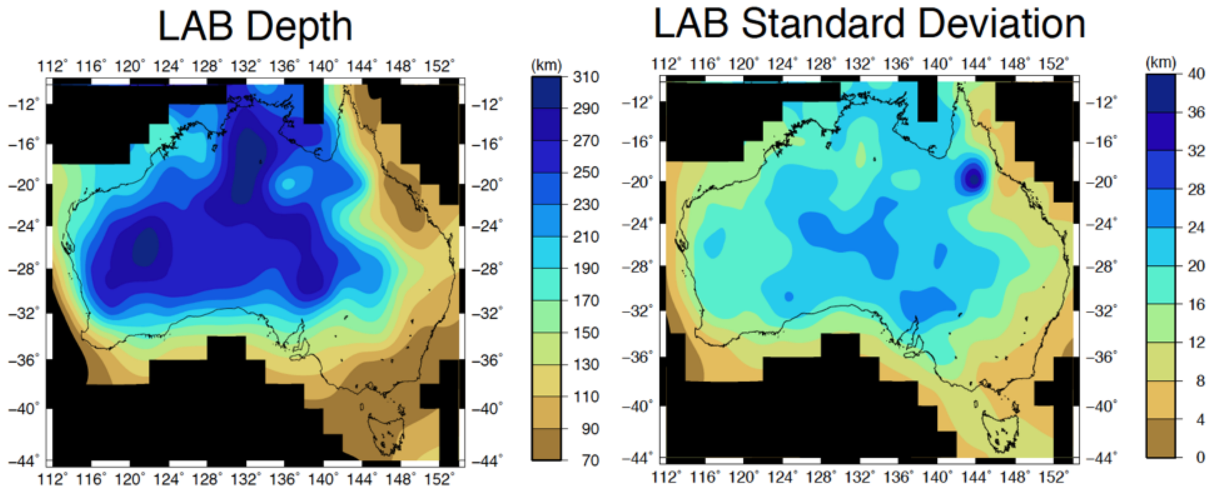

Figure 3.6: A map of depth to Lithosphere-Asthenosphere boundary for Australia (left), with standard deviation (right).

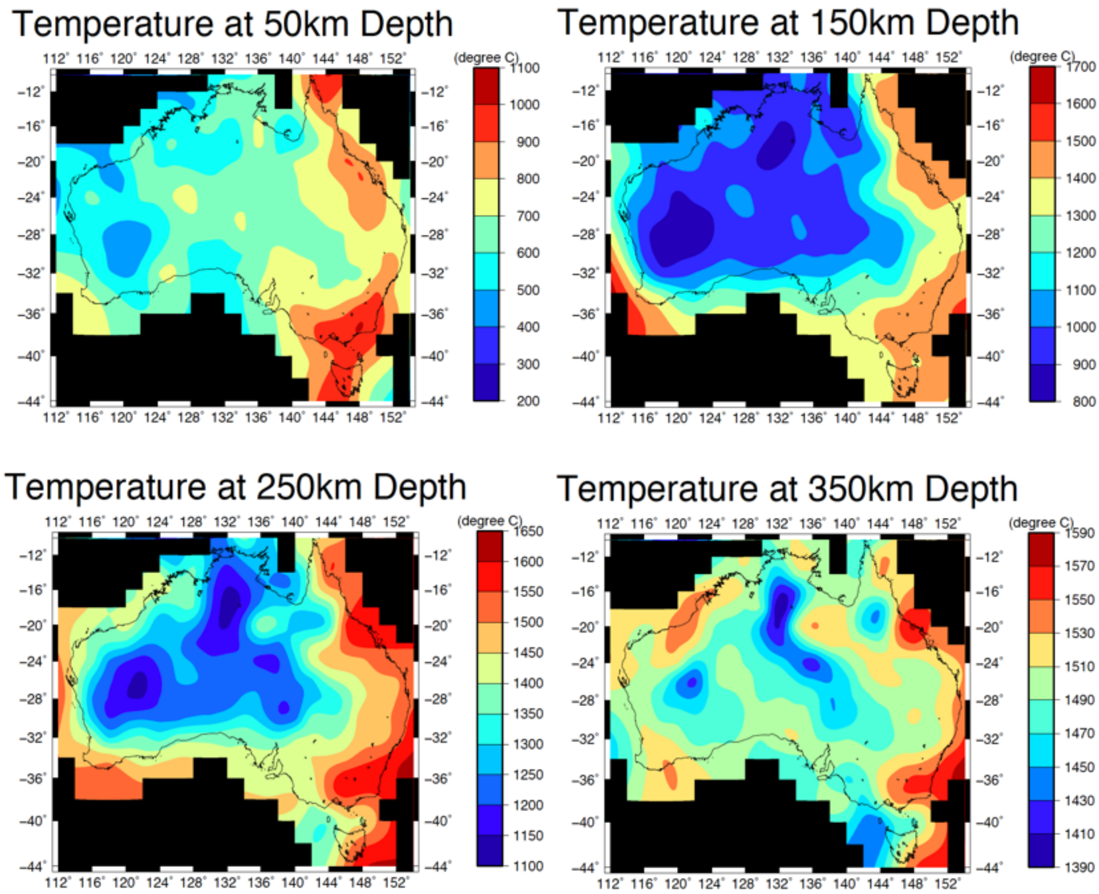

Figure 3.7: Depth slices of temperature model at 50, 150, 250, 350 km.

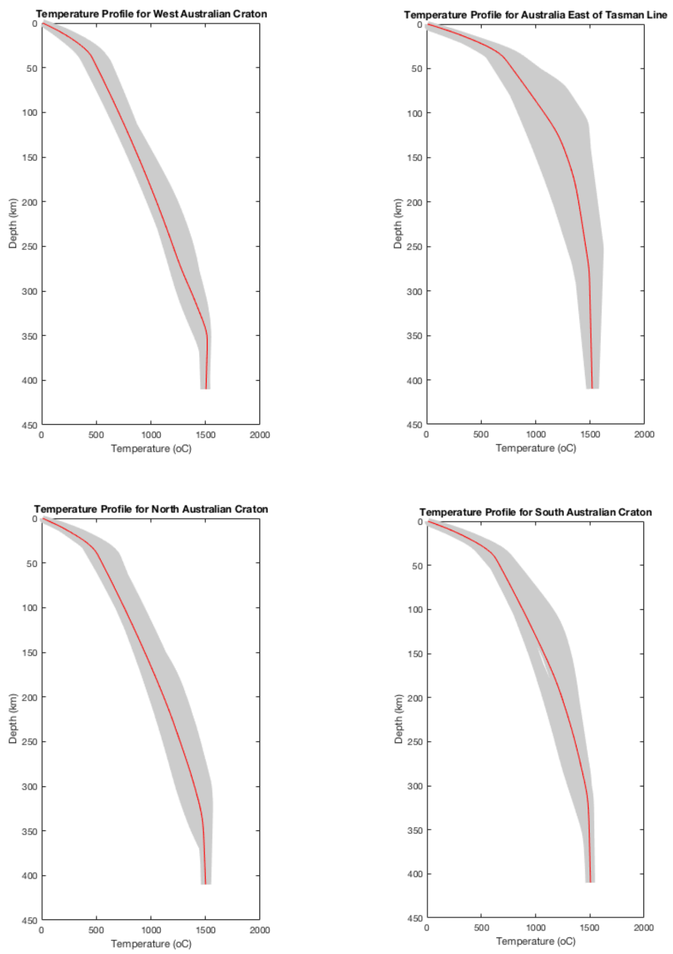

FIGURE 3.8: Temperature profiles for the major cratonic groups (west, east, north) as well as the younger, easternmost third of the continent. The grey area shows the range of temperatures for each region, with the red line indicating the mean temperature profile.

the lithosphere. We emphasise here that these results arise exclusively from the inversion using only geophysical data; no a priori local constrains have been imposed from e.g. xenolith data. Where as, the sub-lithospheric mantle and Phanerozoic lithosphere are enriched in Al_2O_3 and CaO and and have a lower Mg#.

The correlation between composition and lithospheric thickness is one of the more intriguing observations we have made of our models. While finding older (western and central) regions of Australian lithosphere to be chemically depleted, and provinces on the eastern margin to be fertile is not surprising, what's interesting is the correlation between these thin, fertile lithospheric provinces and Cenozoic era volcanism. Along the eastern margin of

Australia resides a 2,000km long hot-spot track (the Cosgrove track), which is believed to be the surface expression of up-welling mantle plumes. A recent study by Davies et al. (2015) found three evident trends along the Cosgrove track: (1) that volcanic gaps occur in regions where lithospheric thickness exceeds $\sim$150km, (2) basaltic volcanoes in central Queensland occur where lithospheric thickness is less than $\sim$110km, (3) and low-volume volcanism in southern NSW/Victoria occurs, exclusively, in regions of intermediate lithospheric thickness. Coincidentally, in our models (Figure 3.9-3.11) these three areas have the highest Al_2O_3 and CaO concentrations and lowest Mg# in the lithosphere, while also happen to coincide with areas of lithospheric thickness that agree with Davies et al. (2015)'s observed correlations. Davies et al. (2015)'s work suggests that the thickness of overlying lithosphere is dictating the volume and composition of plume-derived magmas, by limiting the rise height of the underlying plume and the degree of partial melting.

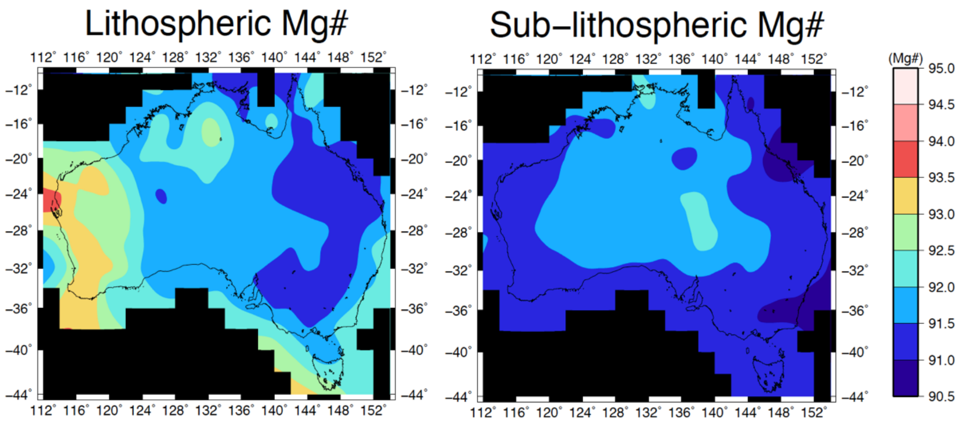

FIGURE 3.9: Mg# in the lithosphere and sub-lithosphere.

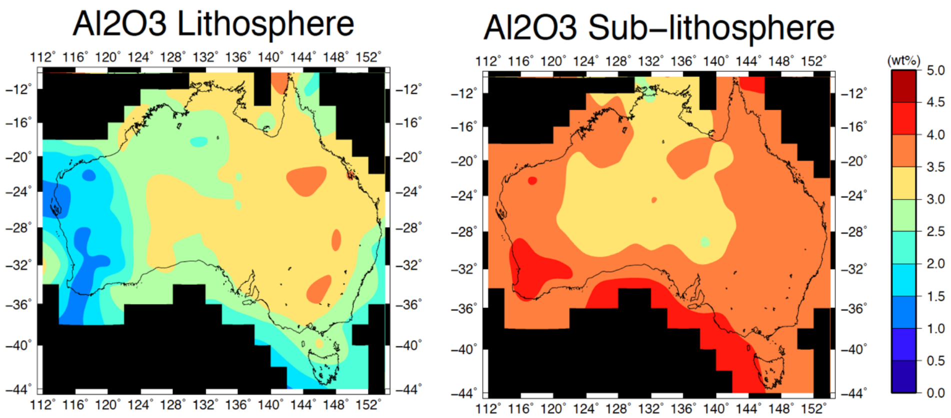

FIGURE 3.10: Al_2O_3 content in the lithosphere and sub-lithosphere.

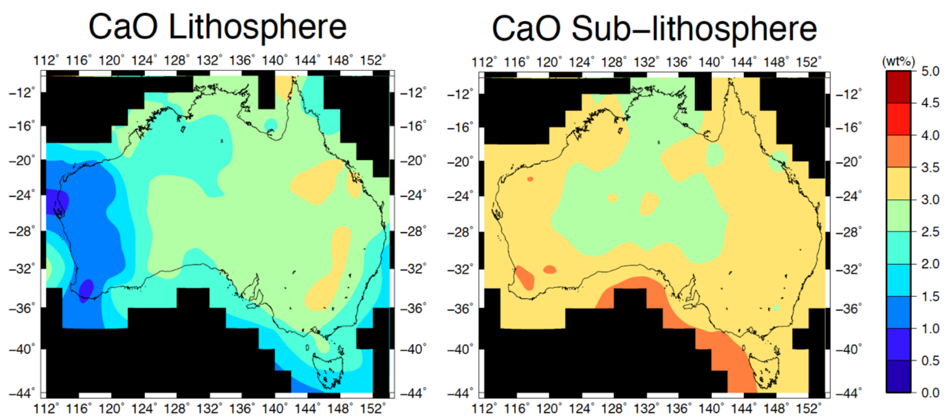

FIGURE 3.11: CaO content in the lithosphere and sub-lithosphere.

4

Discussion

4.1 Method Limitations

Before discussing the promising results from our work we believe it will be beneficial to the reader to be honest about the limitations and caveats of the method first. The most obvious is the fact that this is not a full 3-D inversion, and there is always a level of uncertainty associated with the 1D approximation. The resolution to composition at depths $>\sim$200km is relatively poor if we do not include data on V_p. Although the results are good for most of the lithosphere, that is they correspond well with previous models and show no unexplainable anomalies, we cannot distinguish layering in the lithosphere. In depth studies on the limitations of this method by Afonso et al. (2013b) reveal that only temperature anomalies of $\Delta T >\sim 150°$C and large compositional anomalies ΔMg#>3 (or bulk $\Delta Al_2O_3 > 1.5$) can be expected to be resolved simultaneously when combining high-quality geophysical data.

4.2 Thermochemical Lithospheric Structure of Australia

As seen in Figures 3.9-3.11 we display Mg# (mentioned in 2.5.1 and 3.5.3), Al_2O_3 and CaO results to sufficiently show critical variations within the lithosphere. Briefly mentioned above in section 3.5.3 is a description of the chemical structure of the lithosphere, showing depleted cratonic peridotites have a higher Mg#, with lower Al_2O_3 and CaO concentrations when compared to more fertile Phanerozoic peridotites within the lithosphere. In this way, we can see that West Australian Craton (containing the Yilgarn and Pilbara cratons) is more depleted when compared to the Proterozoic dominated North Australian Craton, with the South Australian Craton (containing the Gawler Craton) the most fertile of the Arachaean Provinces. Comparing these depleted regions to the temperature variations at depths in Figure 3.7 and temperature profiles in Figure 3.8 confirms that older parts of the lithosphere are cold, thick and composed of depleted peridotites.

We find our thermochemical results to be in good agreement with geophysical and geochemical studies by Goes et al. (2005) and Khan et al. (2013). In the following section we provide a direct comparison of these studies to our thermal and chemical estimates. The more recent of the two works by Khan et al. (2013) is a study on the thermochemical structure of the upper mantle, using a similar approach to that used here (e.g. probabilistic inversion of dispersion data), more details on the methodology and parameterisation of their models are given in section 1.1. The results displayed by Khan et al. (2013) are limited to the elemental ratios of Mg/Fe (Figure 1.2) and Mg/Si, as they were found to be the best resolved compositional parameters. From maps of these ratios it is clear that the Archaean and Proterzoic provinces are characterised by high values of Mg/Fe and Mg/Si (to depths of ~250km), compared to the Phanerozoic and oceanic regions. Khan et al. (2013) find these compositional variations in the central and western areas of Australia to be in general agreement with what is expected for depleted peridotite, and hence in agreement with our initial findings on lithospheric chemical structure.

In addition to these chemical estimates, Khan et al. (2013) also provide models of the thermal structure in the lithosphere, the work of Goes et al. (2005) is also relevant to this comparison. The approach of the latter study is fundamentally different to that of the former

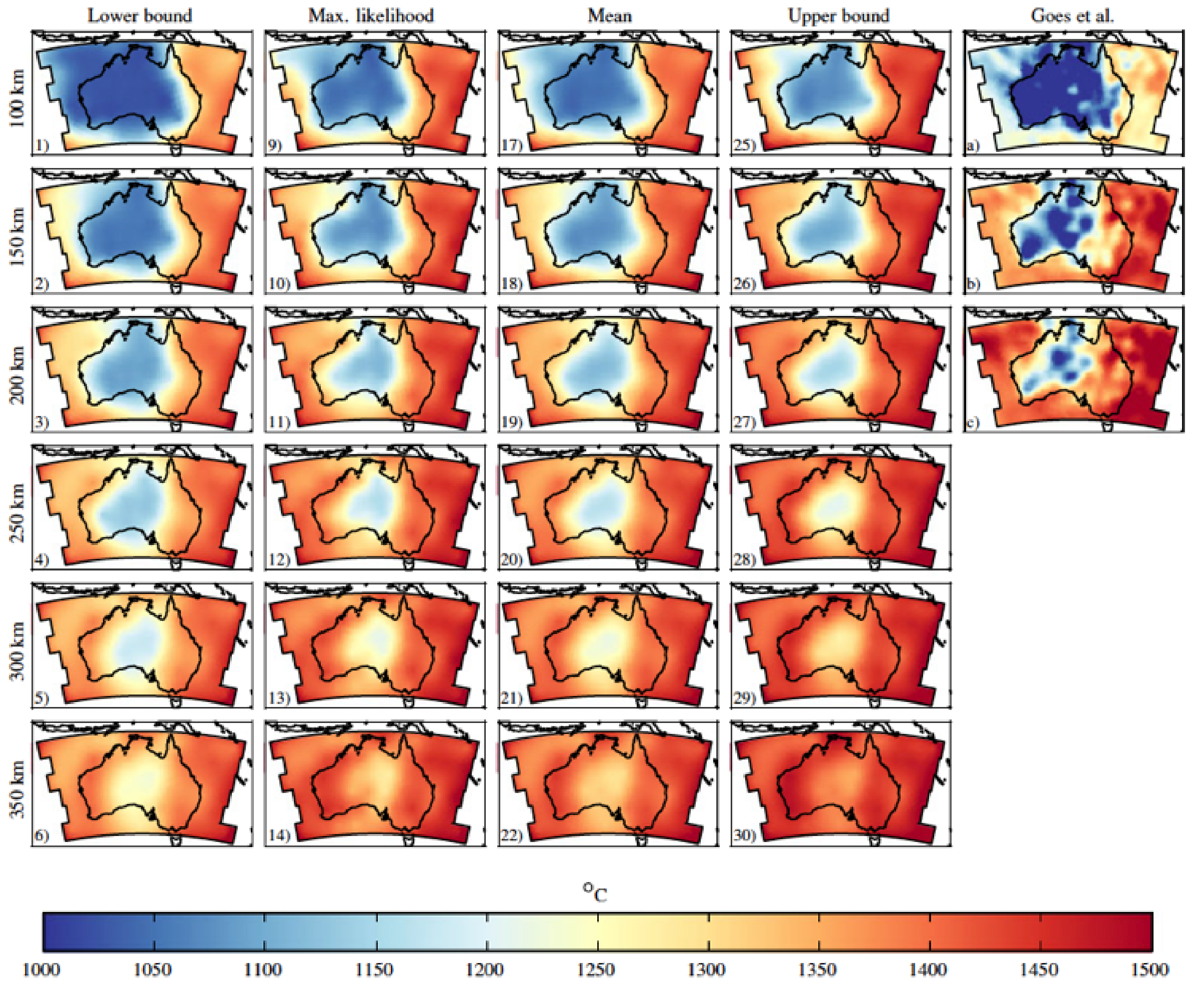

Figure 4.1: Maps of temperature variations in the lithosphere beneath Australia and surrounding oceanic regions. (1-30) are models by Khan et al. (2013). (a-c) thermal maps from Goes et al. (2005).

(and subsequently our own). Goes et al. (2005) are able to derive temperature profiles in the lithosphere underlying Australia by thermal mapping of a seismic tomographic model. Figure 4.1 shows the thermal maps from both these studies, clearly distinguishable within them are the colder Archaean and Proterozoic provinces and the relatively hotter Phanerozoic east. These models are in agreement with our maps of lithospheric temperature variation (Figure 3.7). More defined anomalies are visible in Goes et al. (2005), however due to the difference in approach, we can only say that their models qualitatively agree with our own. Which is to say, temperatures in the range of 800°C-1100°C and 1300°C-1600°C are consistent between the models for cold and hot provinces, respectively. In all these models (including our own) there is a clear correlation between tectonic provinces in the crust and the thermochemical structure in the underlying lithosphere.

4.3 Crustal Component

The Australian Seismic Reference Model (AuSREM): crustal component (Salmon et al., 2012) (more information in section 1.1), provides a high resolution map of the Moho surface, as shown in Figure 4.2. Comparatively, this is in good agreement with our own estimate for Moho depth (Figure 4.2), which shows a thick crust (∼45km) in central Australia and eastern Australia with an average thickness of ∼35km, and the shallowest Moho along the western edge of the continent (∼25-35km). Moho depth estimates are also provided by Khan et al. (2013), and while at a considerably lower resolution, the results also show thick and thin crust in central and western Australia, respectively.

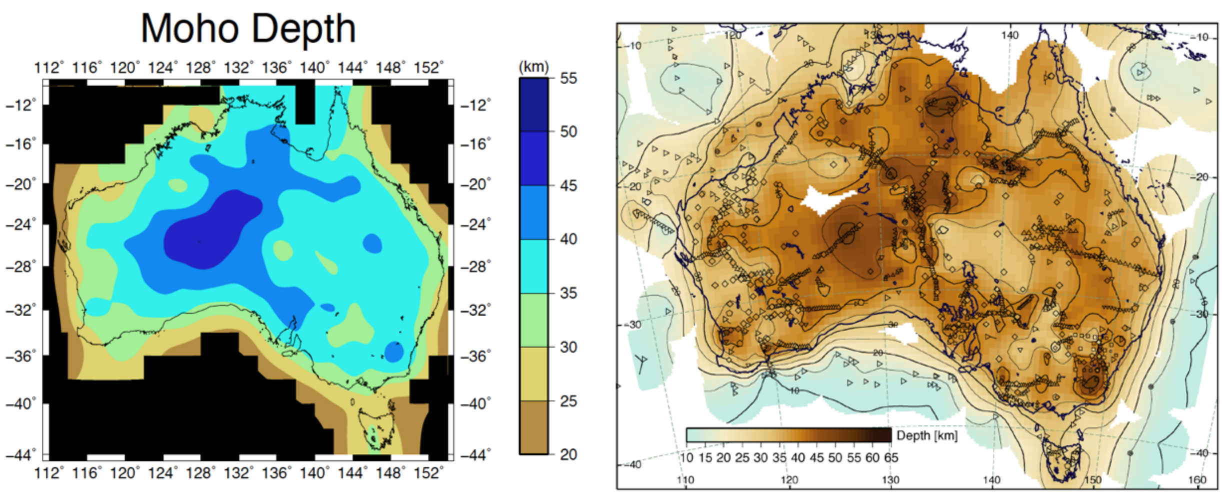

FIGURE 4.2: (Left) Our model for Moho depth. (Right) Reference model from AuSREM (Salmon et al., 2012), the variety of symbols are used to distinguish the various data sources used by Salmon et al. (2012) which can be ignored for out purposes.

4.4 Mantle Component

The depth to the LAB predicted by our inversion is shown in Figure 3.6. In Figure 4.3 we compare the recent estimates of Kennett et al. (2012) and Yoshizawa (2014). It should be noted that Yoshizawa (2014) is the source of the fundamental-mode Rayleigh wave dispersion data used as the primary dataset in our inversion. All models presented here are in excellent agreement that the Archaean and Proterozoic provinces are underlain by the thickest parts of the lithosphere. However there are some discrepancies regarding the maximum depth between our model (~290km) and the estimates provided by Kennett et al. (2012) and Yoshizawa (2014) (~240km). This can be explained by two main factors: the different definitions of LAB adopted in these works and the simple attenuation model used in our inversion. We discuss these further below.

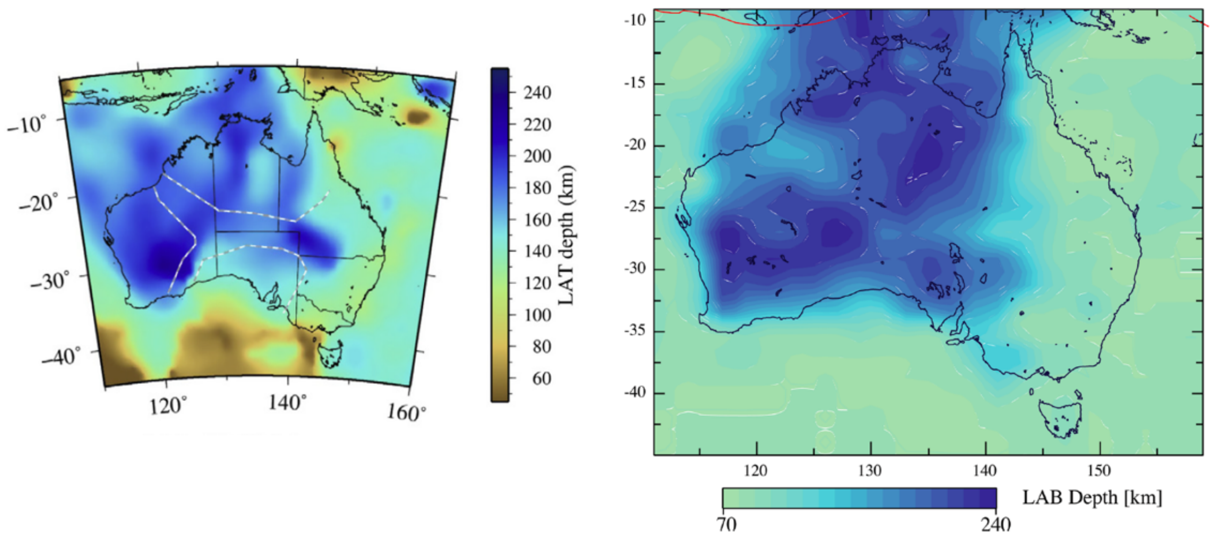

Figure 4.3: (Left) The lower bound of the LAB depth, as given in Yoshizawa (2014). (Right) Estimate of LAB depth from AuSREM (Kennett et al., 2012).

In our work, the LAB is defined as the thermal boundary layer separating the conductive lithosphere, from the convective asthenosphere; from an operational point of view, the actual LAB is defined as the depth to the 1250°C isotherm (see Afonso et al. (2016a) for the rationale). However, in seismic studies (e.g. (Kennett et al., 2012) and (Yoshizawa, 2014)), this definition is based on a gradual decrease in velocity and an increase in attenuation.

Despite these different definitions, the general agreement between these works is remarkable.

Another important factor to consider is that we have adopted a single attenuation model for the entire region. The model is based on the work of Jackson and Faul (2010) and its implementation in the inversion algorithm is fully described in Afonso et al. (2016b). However, there is good evidence that the attenuation properties of the Australian lithospheric mantle are highly variable and those regions with thick lithosphere exhibit very little attenuation compared to those e.g. in the eastern margin (Kennett et al., 2012). Therefore, we expect that our maximum estimates will be slightly overestimated. More complicated and spatially variable attenuation models will have to be considered in the future. However, this is beyond the scope of the present work.

4.5 Velocity and Density Structure

The following Figures 4.4, 4.5 and 4.6 show the P-wave, S-wave and density structure, respectively. In each visualisation we have chosen to show two depths from the shallow crust (at 16 and 26km) and two in the lithospheric mantle (100km and 200km). The crustal structure shows a uniform spatial distribution of anomalous regions between the three data sets, with wave-speed and density increasing with depth. These models show a distribution of values consistent with the AuSREM crustal component (Salmon et al., 2012), and the density field defined by Aitken et al. (2015) for the shallow crust. While the velocity and density values are evenly distributed relative to the lithospheric mantle, we find that the Archaean cratons in western and central Australia are dominated by higher wave-speeds. This is in good agreement with previous tomographic studies (e.g. Saygin and Kennett (2012)) and there are correlations with thicker parts of the crust in these central areas (see section 4.3).

The lithospheric mantle structure in our models shows a clear boundary between Precambrian and Paleozoic provinces that has been observed in seismic studies as early as Debayle et al. (2000). The velocity structure displayed is in good agreement with the models produced by the AuSREM mantle component (Kennett et al., 2012), and studies of shear-waves (e.g. Kennett et al. (2004), Fishwick et al. (2005)) confirm a strong contrast in S-wave speeds is observed beneath western and central Australia and the eastern margin of the continent. The density structure at 200km depth correlates well with the models defined by Aitken et al. (2015), with similar maximum values of $\sim 3450 kg/m^3$. In the West Australian craton fast S-wave speeds (Figure 4.5) are seen beneath and within the Archaean cratons at 100km's depth, however with increasing depth, faster velocities continue beneath the Yilgarn craton and not the Pilbara. A similar anomaly is persistent in the North Australian craton at depths of 200km, suggesting that this Proterozoic dominated province may have some Archaean lithospheric roots (Fishwick et al., 2005).

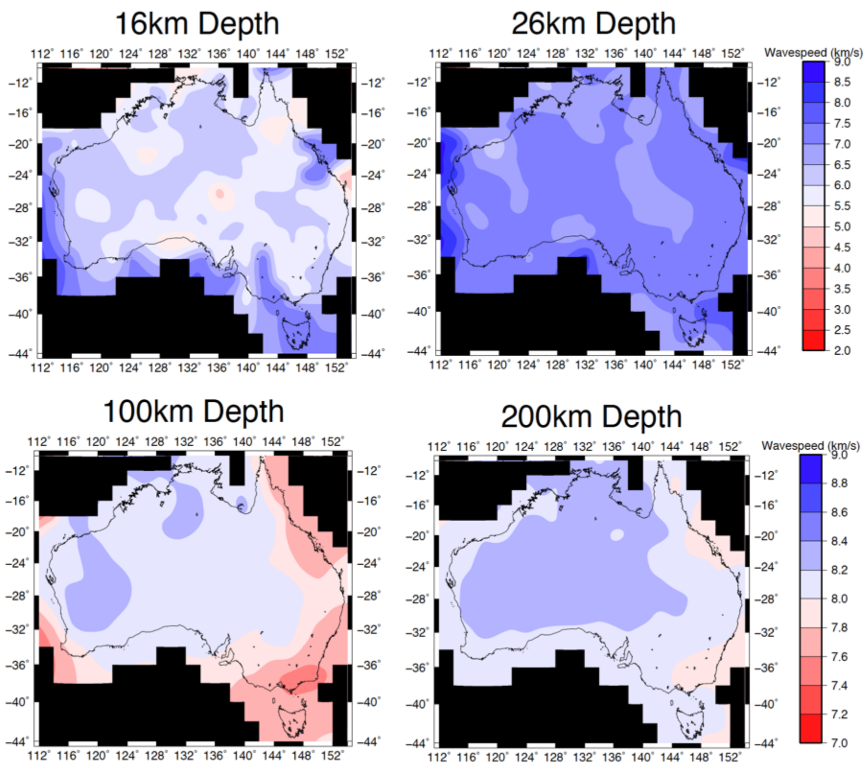

Figure 4.4: P-wave speed at depth slices in the crust (16, 26km) and the mantle (100, 200km).

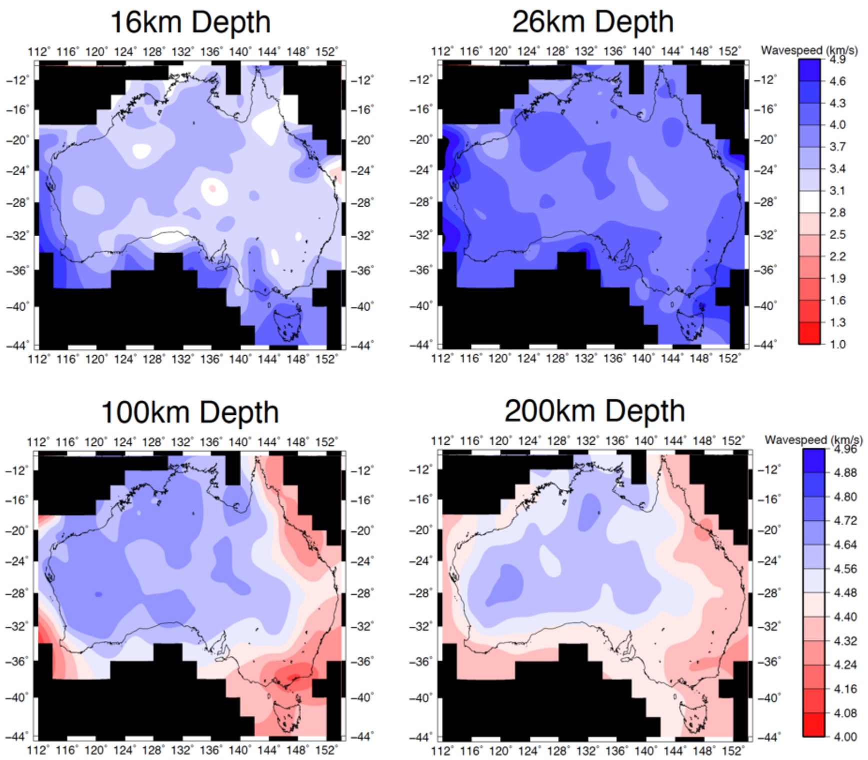

FIGURE 4.5: S-wave speed at depth slices in the crust (16, 26km) and the mantle (100, 200km).

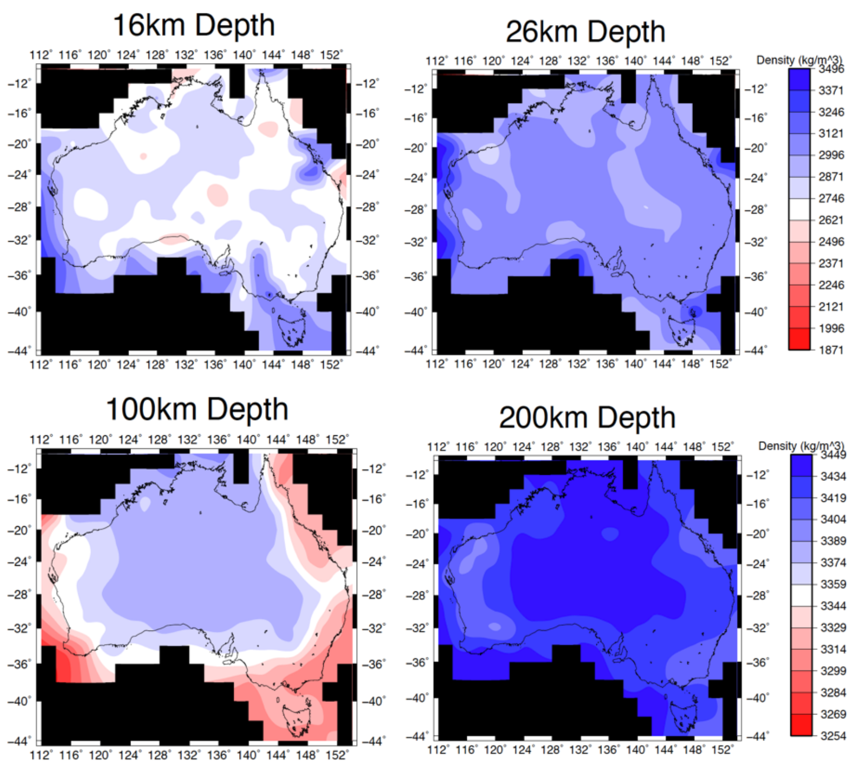

FIGURE 4.6: Density at depth slices in the crust (16, 26km) and the mantle (100, 200km).

5

Conclusions and Future Work

In this thesis, we have employed a multi-observable probabilistic approach (Afonso et al., 2013a,b) to estimate the thermochemical structure of the lithosphere and sub-lithospheric upper mantle beneath the Australian continent by inverting Rayleigh wave dispersion data, geoid height, elevation, surface heat flow and *a priori* crustal information. With this method we obtain 1D approximations of the thermal structure, chemical composition, depth to the Moho and LAB, and velocity and density structure. From these results were are able to reveal the following information about the lithosphere:

1. The crustal structure shows a relatively even distribution of wave-speeds and density values, with moderate highs in S-wave velocity observed in western and central regions. Estimates of Moho depth shows central Australia has the thickest crust (∼45km), with intermediate depths in the easternmost margin (∼35km) and the shallowest Moho

along the western edge of the continent (∼25-35km). These results are in good agreement with previous crustal studies (e.g. Salmon et al. (2012), Saygin and Kennett (2012), Khan et al. (2013)).

2. The depth to the lithosphere-asthenosphere boundary varies greatly between tectonic provinces, with average depths of ∼250km in the North, South and West Australian cratons, coinciding with the oldest parts of the lithosphere. Maximum values in these cratons are slightly larger than that estimated by previous studies (e.g. Kennett et al. (2012), Yoshizawa (2014)). In contrast, the easternmost region of Australia is found to be underlain by significantly thinner lithosphere ∼100km.

3. S-wave speed velocity models in the lithospheric upper mantle show a strong contrast in velocity between western and central Australia, and the easternmost part of the continent, which is observed in previous seismic and tomographic studies (e.g. Kennett et al. (2004), Fishwick et al. (2005), Kennett et al. (2012)). High velocity anomalies at depths of 200km have implications that the Proterozoic North Australian craton may have similar lithospheric roots to the Archaean (Yilgarn) craton in Western Australian (as put forward in Fishwick et al. (2005)).

4. We find that chemically depleted cratonic peridotites have a higher Mg# (∼93), with lower Al_2O_3 and CaO concentrations when compared to the more fertile sub-lithospheric mantle and Phanerozoic peridotites within the lithosphere. Comparing these depleted regions to temperature variations at depths and temperature profiles confirms that older parts of the lithosphere are cold, thick and composed of depleted peridotites. These thermochemical results are in good agreement with other estimates of this structure (e.g. Goes et al. (2005), Khan et al. (2013)). A comparison of these collective studies indicates that there is a strong correlation between tectonic provinces and the thermochemical structure in the lithosphere.

5. Intriguing correlations between lithospheric thickness and Cenozoic era volcanism are drawn by Davies et al. (2015), and supported by our models. Lithospheric thickness may by responsible for the volume and composition of mantle-derived magmas in a

hot-spot track situated in eastern Australia.

Although the results from our inversion process are of high-resolution, good quality and correlate well with a variety of similar studies, they are only 1-D approximations and as such always carry a level of uncertainty with them. The future for this preliminary work involves the implementation of the full 3-D multi-observable probabilistic inversion method (Afonso et al., 2013a,b), which uses these 1-D results as inputs for the next stage. This kind of work can provide further insights into the complex thermochemical structure of the Australian lithosphere and improve upon the findings made here.

References

JC Afonso, M Fernandez, G Ranalli, WL Griffin, and JAD Connolly. Integrated geophysical-petrological modeling of the lithosphere and sublithospheric upper mantle: Methodology and applications. *Geochemistry, Geophysics, Geosystems*, 9(5), 2008.

JC Afonso, G Ranalli, M Fernàndez, WL Griffin, SY O'Reilly, and U Faul. On the vp/vs–mg# correlation in mantle peridotites: Implications for the identification of thermal and compositional anomalies in the upper mantle. *Earth and Planetary Science Letters*, 289 (3):606–618, 2010.

JC Afonso, J Fullea, WL Griffin, Y Yang, AG Jones, JA D Connolly, and SY O'Reilly. 3-d multiobservable probabilistic inversion for the compositional and thermal structure of the lithosphere and upper mantle. i: A priori petrological information and geophysical observables. *Journal of Geophysical Research: Solid Earth*, 118(5):2586–2617, 2013a.

JC Afonso, J Fullea, Y Yang, JAD Connolly, and AG Jones. 3-d multi-observable probabilistic inversion for the compositional and thermal structure of the lithosphere and upper mantle. ii: General methodology and resolution analysis. *Journal of Geophysical Research: Solid Earth*, 118(4):1650–1676, 2013b.

JC Afonso, M Moorkamp, and J Fullea. Imaging the lithosphere and upper mantle: where we are at and where we are going. *Integrated Imaging of the Earth: Theory and Applications, Geophysical Monograph*, 218:191–218, 2016a.

JC Afonso, N Rawlinson, Y Yang, DL Schutt, AG Jones, J Fullea, and WL Griffin. 3-d multiobservable probabilistic inversion for the compositional and thermal structure of the lithosphere and upper mantle: Iii. thermochemical tomography in the western-central us. *Journal of Geophysical Research: Solid Earth*, 121(10):7337–7370, 2016b.

ARA Aitken, C Altinay, and L Gross. Australia's lithospheric density field, and its isostatic equilibration. *Geophysical Supplements to the Monthly Notices of the Royal Astronomical Society*, 203(3):1961–1976, 2015.

C Amante and BW Eakins. Etopo1 1 arc-minute global relief model: Procedures, data sources and analysis. *National Geophysical Data Center, NOAA*, 2009.

PG Betts, D Giles, GS Lister, and LR Frick. Evolution of the australian lithosphere. *Australian Journal of Earth Sciences*, 49(4):661–695, 2002.

SF Chen, JW Libby, JE Greenfield, S Wyche, and A Riganti. Geometry and kinematics of large arcuate structures formed by impingement of rigid granitoids into greenstone belts during progressive shortening. *Geology*, 29(3):283–286, 2001.

WJ Collins, Van Kranendonk, MJ, and C Teyssier. Partial convective overturn of archaean crust in the east pilbara craton, western australia: driving mechanisms and tectonic implications. *Journal of Structural Geology*, 20(9):1405–1424, 1998.

JAD Connolly. Computation of phase equilibria by linear programming: a tool for geodynamic modeling and its application to subduction zone decarbonation. *Earth and Planetary Science Letters*, 236(1):524–541, 2005.

DR Davies, Nicholas Rawlinson, Giampiero Iaffaldano, and IH Campbell. Lithospheric controls on magma composition along earth/'s longest continental hotspot track. *Nature*, 525 (7570):511–514, 2015.

E Debayle, , and BLN Kennett. The australian continental upper mantle: structure and deformation inferred from surface waves. *Journal of Geophysical Research: Solid Earth*, 105(B11):25423–25450, 2000.

L Eppelbaum, I Kutasov, and A Pilchin. *Applied Geothermics*. Springer, 2014.

MA Etheridge, RWR Rutland, and LAI Wyborn. Orogenesis and tectonic process in the early to middle proterozoic of northern australia. *Proterozic Lithospheric Evolution*, pages 131–147, 1987.

S Fishwick, BLN Kennett, and AM Reading. Contrasts in lithospheric structure within the australian craton?insights from surface wave tomography. *Earth and Planetary Science Letters*, 231(3):163–176, 2005.

S Goes, FJ Simons, and K Yoshizawa. Seismic constraints on temperature of the australian uppermost mantle. *Earth and Planetary Science Letters*, 236(1):227–237, 2005.

DR Gray and DA Foster. Character and kinematics of faults within the turbidite-dominated lachlan orogen: implications for tectonic evolution of eastern australia. *Journal of Structural Geology*, 20(12):1691–1720, 1998.

Z Guo, JC Afonso, MT Qashqai, Yi Yang, and YJ Chen. Thermochemical structure of the north china craton from multi-observable probabilistic inversion: Extent and causes of cratonic lithosphere modification. *Gondwana Research*, 37:252–265, 2016.

H Haario, E Saksman, and J Tamminen. An adaptive metropolis algorithm. *Bernoulli*, 7 (2):223–242, 2001.

H Haario, M Laine, A Mira, and E Saksman. Dram: efficient adaptive mcmc. *Statistics and Computing*, 16(4):339–354, 2006.

RB Herrmann. Computer programs in seismology: An evolving tool for instruction and research. *Seismological Research Letters*, 84(6):1081–1088, 2013.

I Jackson and UH Faul. Grainsize-sensitive viscoelastic relaxation in olivine: Towards a robust laboratory-based model for seismological application. *Physics of the Earth and Planetary Interiors*, 183(1):151–163, 2010.

BLN Kennett, S Fishwick, AM Reading, and N Rawlinson. Contrasts in mantle structure beneath australia: relation to tasman lines? *Australian Journal of Earth Sciences*, 51(4): 563–569, 2004.

BLN Kennett, A Fichtner, S Fishwick, and K Yoshizawa. Australian seismological reference model (ausrem): mantle component. *Geophysical Journal International*, 192(2):871–887, 2012.

A Khan, A Zunino, and F Deschamps. Upper mantle compositional variations and discontinuity topography imaged beneath australia from bayesian inversion of surface-wave phase velocities and thermochemical modeling. *Journal of Geophysical Research: Solid Earth*, 118(10):5285–5306, 2013.

G Laske, G Masters, Z Ma, and M Pasyanos. Update on crust1.0 - a 1-degree global model of earth's crust. *EGU General Assembly 2013*, 2013.

EC Leitch and PA Cawood. Provenance determination of volcaniclastic rocks: the nature and tectonic significance of a cambrian conglomerate from the new england fold belt, eastern australia. *Journal of Sedimentary Research*, 57(4), 1987.

LR Lines and S Treitel. Tutorial: A review of least-squares inversion and its application to geophysical problems. *Geophysical prospecting*, 32(2):159–186, 1984.

S Malcolm. Geophysical inversion with a neighbourhood algorithm - ii. appraising the ensemble. *Geophysical Journal International*, 138(3):727–746, 1999.

W Menke. *Geophysical data analysis: discrete inverse theory: MATLAB edition*, volume 45. Academic press, 2012.

N Metropolis, AW Rosenbluth, MN Rosenbluth, AH Teller, and E Teller. Equation of state calculations by fast computing machines. *The journal of chemical physics*, 21(6):1087–1092, 1953.

A Mira. On metropolis-hastings algorithms with delayed rejection. *Metron*, 59(3-4):231–241, 2001.

K Mosegaard and A Tarantola. Monte carlo sampling of solutions to inverse problems. *Journal of Geophysical Research: Solid Earth*, 100(B7):12431–12447, 1995.

JS Myers. Precambrian history of the west australian craton and adjacent orogens. *Annual Review of Earth and Planetary Sciences*, 21(1):453–485, 1993.

NK Pavlis, SA Holmes, SC Kenyon, and JK Factor. The development and evaluation of the earth gravitational model 2008 (egm2008). *Journal of Geophysical Research: Solid Earth*, 117(B4), 2012.

MT Qashqai. *Multi-observable probabilistic inversion for the thermochemical structure of the lithosphere*. PhD thesis, Macquarie University, December 2016.

M Salmon, BLN Kennett, and E Saygin. Australian seismological reference model (ausrem): Crustal component. *Geophysical Journal International*, 192(1):190–206, 2012.

WN Sawka and BW Chappell. The distribution of radioactive heat production in i-and s-type granites and residual source regions: Implications to high heat flow areas in the lachlan fold belt, australia. *Australian Journal of Earth Sciences*, 33(2):107–118, 1986.

E Saygin and BLN Kennett. Crustal structure of australia from ambient seismic noise tomography. *Journal of Geophysical Research: Solid Earth*, 117(B1), 2012.

JA Scales and R Snieder. To bayes or not to bayes? *Geophysics*, 62(4):1045–1046, 1997.

B Shan, JC Afonso, Y Yang, CJ Grose, Y Zheng, X Xiong, and L Zhou. The thermochemical structure of the lithosphere and upper mantle beneath south china: Results from multi-observable probabilistic inversion. *Journal of Geophysical Research: Solid Earth*, 119(11): 8417–8441, 2014.

FJ Simons, RD Van Der Hilst, J Montagner, and A Zielhuis. Multimode rayleigh wave inversion for heterogeneity and azimuthal anisotropy of the australian upper mantle. *Geophysical Journal International*, 151(3):738–754, 2002.

A Tarantola. *Inverse problem theory and methods for model parameter estimation*. SIAM, 2005.

A Tarantola and B Valette. Generalized nonlinear inverse problems solved using the least squares criterion. *Reviews of Geophysics*, 20(2):219–232, 1982a.

A Tarantola and B Valette. Inverse problems = quest for information. *Journal of Geophysics*, 50(3):150–170, 1982b.

IM Tyler and TJ Griffin. Structural development of the king leopold orogen, kimberley region, western australia. *Journal of Structural Geology*, 12(5-6):703–714, 1990.

K Yoshizawa. Radially anisotropic 3-d shear wave structure of the australian lithosphere and asthenosphere from multi-mode surface waves. *Physics of the Earth and Planetary Interiors*, 235:33–48, 2014.

K Yoshizawa and BLN Kennett. Multimode surface wave tomography for the australian region using a three-stage approach incorporating finite frequency effects. *Journal of Geophysical Research: Solid Earth*, 109(B2), 2004.

TE Zegers, SH White, M De Keijzer, and PGHM Dirks. Extensional structures during deposition of the 3460 ma warrawoona group in the eastern pilbara craton, western australia. *Precambrian Research*, 80(1-2):89–105, 1996.